Examination of the ground states of topological superconductors in the presence of strong interactions

Botond OSVÁTH

MSc Thesis

Supervisors: László OROSZLÁNY and Gergely BARCZA

Eötvös Loránd University

Department of Physics of Complex Systems

Contents

1 Introduction

The concept of topological phases has become one of the central constituents in condensed matter physics [1–6], as it provides a fundamentally new way for the classification of physical systems. The most essential idea behind this classification is the bulk-boundary correspondence [7], which connects the topology of the bulk to the existence of localized edge states. These edge states are extraordinarily robust against disorder, and they show special properties, for example they can be perfectly transmitting channels in the case of Chern insulators or time-reversal symmetric two-dimensional topological insulators. They also have a wide variety of applications, for example a new way to measure physical constants [8] or to create an all-electrical detection method of spin polarization [9].

Quantum computing is amongst the most rapidly developing areas in physics, as it would make certain computational tasks exponentially faster. This increase in speed would be beneficial in a host of applications relevant to everyday life, for example it would accelerate medicine development, improve battery efficiency, optimize logistical problems and make possible better AI classification [10]. Thanks to this huge attention, we are getting closer and closer to the desired goal [11], but there is still a long way to go [12], for example we need find a way to reduce the fragility of the quantum states due to decoherence and to eliminate the high error rate of the gates manipulating qubits.

The aforementioned two research fields might seem distant at first glance, but it has already been shown that topological superconductivity, in theory, is useful in storing and manipulating quantum information in a robust and noise-resiliant way [13–16]. Thanks to this realization, there has been development in both theoretical [17] and experimental [18,19] topological quantum computing, however, but there are still a lot of open problems.

There are two major ways of realizing topological qubits: either by using "regular" materials with special interactions so that it gives rise to topological protection [20,21], or by using topological materials. For our research, the relevant one is the second, hence we are detailing that one only. One possibility is to use nanowires [18,22]. A viable experimental setup from [18] is shown in Figure 1, where a semiconducting nanowire is in proximity to an s-wave superconductor. The system is subject to an external magnetic field B. Crucially Rashba type spin-orbit coupling, acting like an effective momentum-dependent

perpendicular magnetic field B_{SO} is also present. The interplay of superconductivity, the external magnetic field, and spin-orbit coupling results in the stabilization of Majorana fermions at the edge of the wire.

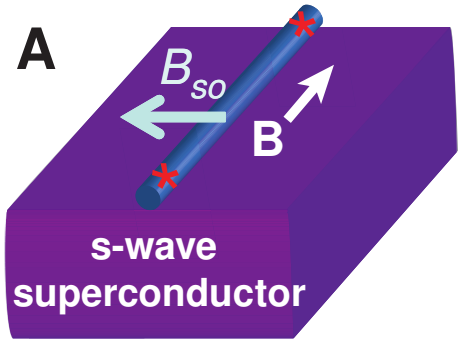

Figure 1: Possible experimental setup of implementing a topological qubit. A semiconducting nanowire in proximity to an s-wave superconductor. An external B field applied parallel to the wire. The momentum-dependent Rashba spin-orbit interaction is taken into account by a perpendicular effective magnetic field B_{SO}. The red stars indicate the expected locations of the Majorana zero modes. Figure was taken from [18].

The other path is to use the edge states of topological insulators. The simplest implementation uses Majorana zero modes appearing in a topological insulator due to superconducting proximity effect [23–29]. The number of quantum operations that can be performed with Majorana zero modes under topological protection is limited [15]. However, it turns out that a broader generalization of the Majoranas, the so-called parafermions, can extend the possible operations greatly [30]. Figure 2 illustrates three different experimental setups for realizing parafermions.

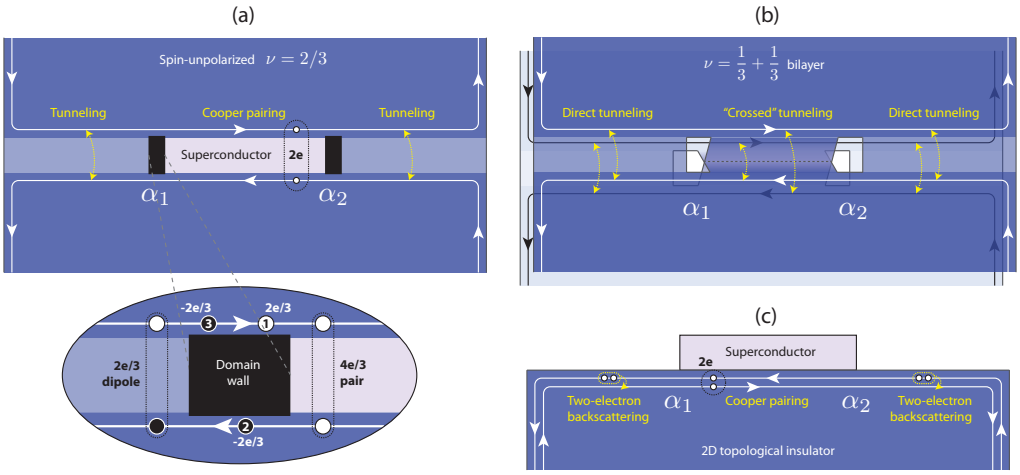

Figure 2: Blueprints for experimental realization of parafermionic zero-modes. Figure was taken from [30].

The first configuration, shown in Figure 2 (a) [31, 32], has two spin-unpolarized 2/3 fractional quantum Hall materials, with a trench between them, containing a superconductor. The trench is thin enough so that it allows tunneling between the two parts, which can open a gap. The superconductor will also open a gap, because of Cooper pairing, but it is quite different. Because of the different nature of the gaps, we can expect parafermions to arise at the domain walls.

The second setup, displayed in Figure 2 (b) [33, 34], has two layers of 1/3 fractional quantum Hall materials, with a trench between them. Similarly to the previous case, the trench is thin so that tunneling is possible between the layers. At the sides, the gap is provided by the tunneling between the same layers, and in the middle, instead of the superconductor, we have "crossed" tunneling (i.e. the electrons are moving between layers).

In the third configuration, seen in Figure 2 (c) [35], the main part is a two-dimensional topological insulator. Again, the edges are gapped in two, fundamentally different ways: with two-electron backscattering in one part, and Cooper pairing due to the proximity of a superconductor on the other one. This setup is fundamentally different from the previous two, as a magnetic field is a core component of them (due to the quantum Hall effect requiring magnetic field), while it is not present in this one. The consequence of this is the explicit time reversal symmetry breaking in the first two model, and the lack of it in the third.

In topological systems, the quantum information is typically stored in low-energy excitations. They are usually linked to defects and interfaces, where they are localized at, and protected by the symmetries of the system, like by time reversal symmetry, particle-hole symmetry or chiral symmetry. The movement of these defects and interfaces around each other (usually referred to as "braiding" in the literature) can realize quantum gates acting on the logical qubits in the degenerate subspace [36–38].

In the present work, our aim is to create a microscopic model of the third configuration shown in Figure 2 (c), which can be effectively solved numerically in terms of Matrix Product States. Our choice fell on this setup because the previously mentioned topological protection due to the time reversal symmetry. Similar systems have already been examined before, but it was done with bosonization [35, 39], which is viable in describing the low-energy states, but the excited states are out of its reach. However, these excited states are taking an important role in, for example, the description of the mechanisms causing decoherence during the movements of interfaces. The understanding of these mechanisms is important, as this braiding is essential to the protected quantum operations.

2 Theoretical background

In this section, we cover the theoretical background necessary for our research. We discuss the Bogoliubov-de Gennes transformation, a tool for treating a quadratic (in the creation/annihilation operator) many-body Hamiltonian with the toolset developed for single particle problems. We introduce the Majorana zero modes and their generalizations, the parafermions and discuss physical systems when they appear. We describe the Bernevig–Hughes–Zhang (BHZ) model, a microscopic lattice model which is able to capture the essential properties of time reversal invariant topological insulators, and show its relevant properties.

2.1 Bogoliubov-de Gennes transformation

One of the key ingredients to the systems we were investigating is the superconductivity, hence in this subsection we are covering it's effective treatment by the Bogoliubov-de Gennes (BdG) transformation. In the presented Hamiltonians, superconductivity is induced by the proximity effect. Here, we are not specifying the source of of the pair potential that's responsible for the process. Experimentally, this is equivalent to putting a superconductor close to system, as it is done in Figure 2.

Let us assume that we have a system with on-site potential, hopping, chemical potential, and Cooper-pair creation/annihilation. The Hamiltonian of the system takes the form

$$H = \sum_{m,l=1}^{N} c_m^\dagger h_{ml} c_l + \left(\sum_{m=2}^{N} \sum_{l=1}^{m-1} c_m^\dagger \hat{\Delta}_{ml} c_l^\dagger + \text{h.c.} \right). \tag{1}$$

Note that in this formula, we don't distinguish between internal and external degrees of freedom, the m and l indices are a given enumeration of those.

We can rewrite it as

$$H = \frac{1}{2} C^\dagger \mathscr{H} C + \frac{1}{2} \operatorname{Tr} h, \tag{2}$$

where $\mathscr{H}$ is the so-called Bogoliubov-de Gennes Hamiltonian,

$$\mathscr{H} = \begin{bmatrix} h & \hat{\Delta} \\ -\hat{\Delta}^* & -h^* \end{bmatrix}, \tag{3}$$

and C is the vector containing the c and $c^\dagger$ operators (and they are the vectors containing the c_i and the $c_i^\dagger$ operators respectively),

$$C = \begin{bmatrix} c \\ c^\dagger \end{bmatrix} = \left[c_1, \ldots, c_N, c_1^\dagger, \ldots, c_N^\dagger\right]^t. \tag{4}$$

The BdG Hamiltonian can be diagonalized as

$$\mathscr{H} \begin{bmatrix} u_n^* \\ v_n^* \end{bmatrix} = E_n \begin{bmatrix} u_n^* \\ v_n^* \end{bmatrix} \quad \text{and} \quad \mathscr{H} \begin{bmatrix} v_n \\ u_n \end{bmatrix} = -E_n \begin{bmatrix} v_n \\ u_n \end{bmatrix} \tag{5}$$

for $n \in \{x | x \in \mathbb{N}_+ \wedge x \leqslant N\}$, with $E_n \geqslant 0$. With these eigenvectors, we can write the eigenmodes d of the system as particle-hole superpositions

$$d_n = \sum_{m=1}^{N} u_{nm} c_m + v_{nm} c_m^\dagger, \tag{6}$$

and the ground state energy is

$$E_{\mathrm{GS}} = \frac{1}{2}\left(\operatorname{Tr} h - \sum_{n=1}^{N} E_n \right). \tag{7}$$

With these, we can finally write the Hamiltonian as

$$H = \sum_{n=1}^{N} E_n d_n^\dagger d_n + E_{\mathrm{GS}}. \tag{8}$$

The ground state can be found from any initial state $|\Psi\rangle$, with removing all of the excitations $d_N \cdots d_1 |\Psi\rangle$, as this process will give either the ground state $|\mathrm{GS}\rangle$ or 0. Then, from the ground state, we can construct the excited states as

$$|n_N, \ldots, n_1\rangle = d_N^{n_N} \cdots d_1^{n_1} |\mathrm{GS}\rangle \tag{9}$$

with energy

$$E_{(n_1,\ldots,n_N)} = E_{\mathrm{GS}} + n_1 E_1 + \ldots + n_N E_N \tag{10}$$

for $n_i \in \{0, 1\} \forall i$.

There is also a slightly different basis: the "position-first-particle-hole-second basis", which can be easily obtained with a basis transformation (in this special case, it is just a permutation). In this basis, with a slight abuse of notation, we write C as

$$C = \left[c_1^\dagger, c_1, c_2^\dagger, c_2, \ldots, c_N^\dagger, c_N\right]^t. \tag{11}$$

This form is more convenient, for example when we want to Fourier transform a translationally invariant BdG Hamiltonian. Another benefit of this basis is that the naturally arising symmetry of every BdG Hamiltonian, the particle-hole symmetry, has a simple form

$$P = I \otimes \sigma_x K, \tag{12}$$

where I is the $N \times N$ identity matrix, and K is the usual complex conjugation in real space.

2.2 Majorana zero modes in the Kitaev wire

One of the simplest Hamiltonians of the form (1) is the so-called Kitaev wire [13]. It is a one-dimensional chain, with nearest-neighbour hopping, but without spin. Due to this simplicity, the Cooper-pair creation/annihilation in the most simplest case has to happen on neighbouring sites as well. Mathematically speaking, this is equivalent to having the coefficients in the form

$$h_{m,l} = -\mu\delta_{m,l} + w\left(\delta_{m+1,l} + \delta_{m-1,l}\right) \tag{13}$$

and

$$\hat{\Delta}_{m,l} = \Delta\delta_{m,l+1}, \tag{14}$$

where μ is the chemical potential, w is the hopping and Δ is the strength of the pair potential.

Putting it together, we have the Kitaev Hamiltonian

$$H_{\mathrm{K}} = -\mu\sum_{m=1}^{N} c_m^\dagger c_m + \left(w\sum_{m=1}^{N-1} c_m^\dagger c_{m+1} + \Delta\sum_{m=1}^{N-1} c_{m+1}^\dagger c_m^\dagger + \mathrm{h.c.}\right). \tag{15}$$

Let us consider the limit when when $\mu = 0$, $w = \Delta = 1$. The corresponding Hamiltonian reads

$$H_{\mathrm{K,\,fd}} = \sum_{m=1}^{N-1} c_m^\dagger c_{m+1} + \sum_{m=1}^{N-1} c_{m+1}^\dagger c_m^\dagger + \mathrm{h.c.}. \tag{16}$$

At this point, we can introduce the so-called Majorana operators

$$\gamma_{2p-1} = \frac{c_p^\dagger + c_p}{\sqrt{2}} \text{ and } \gamma_{2p} = \frac{c_p^\dagger - c_p}{\sqrt{2}i} \tag{17}$$

for $p = 1, \ldots, N$. They obey $2\gamma_k^2 = 1$, they are their own anti-particle, i.e. $\gamma_k^\dagger = \gamma_k$, and they have fermionic commutation relations: $\gamma_k\gamma_l = -\gamma_l\gamma_k$ (for $k, l = 1, \ldots, 2N$ and $l \neq k$). Using these newly introduced operators, (16) can we rewritten as

$$H_{\text{K, fd}} = -2i \sum_{m=1}^{N-1} \gamma_{2m+2}\gamma_{2m-1}. \tag{18}$$

This is an interesting form, as every term contains operators from different sites. It is also clear that we have pairs of Majorana sites, without any interaction between different pairs. This is why we call this limit the "fully dimerized limit" Another notable property of this form is that there are two γ operators are missing, namely γ_2 and γ_{2N-1}. From these two Majorana operators, we can create a fermionic operator as

$$d_M = \frac{\gamma_{2N-1} + i\gamma_2}{\sqrt{2}}, \tag{19}$$

which has a serious consequence: every state is (at least) twice-degenerate, as the Hamiltonian is independent of this operator.

We can also see this degeneracy from the BdG point of view. The BdG Hamiltonian $\mathscr{H}_{\text{K, fd}}$, in the position-first-particle-hole-second basis, has two zero energy eigenstates:

$$\Psi_1 = \frac{1}{\sqrt{2}} \begin{bmatrix} -i \\ i \\ 0 \\ \ldots \\ 0 \end{bmatrix} \quad \text{and} \quad \Psi_N = \frac{1}{\sqrt{2}} \begin{bmatrix} 0 \\ \ldots \\ 0 \\ 1 \\ 1 \end{bmatrix}. \tag{20}$$

These states have the previously introduced γ_2 and γ_{2N-1} as their creation operator. With this formalism, we can see that they are even more special, as they are their own particle-hole partners. Because of these two properties, they are called Majorana Zero Modes (MZM).

However, as we discussed it before, these γ are self-adjoint, so they cannot be fermionic excitations! Does it mean that two of the eigenmodes of the BdG Hamiltonian are not fermionic? No, because from these two non-fermionic operators, we can create the appropriate fermionic zero energy operators, d_M and its conjugate $d_M^\dagger$. From this procedure, the double degeneracy is even more conspicuous, since for a given state ψ we can either add or remove the zero-energy excitation to get a different (non-zero) state.

We've only seen the fully dimerized Kitaev wire, which is a special case only, so the next step could be to examine a more general case. It turns out that the Majorana Zero Modes will still be present if we go away from the fully dimerized limit (without closing the gap), or if we add a quadratic disorder, and they will still be localized to one side of the wire, but they will have an exponential decay towards the middle.

2.3 Parafermions in the clock model

In this subsection, we introduce the parafermions, the generalizations of the Majorana modes. The introduction will follow the review by Alicea and Fendley [30]: we will start by the generalized quantum clock models, then introduce parafermionic operators and finally draw connection between Majorana fermions and parafermions.

If we take the k-dimensional quantum clock model, which is a generalization of the transverse field Ising-model, with length N

$$H_{\text{clock}} = -J \sum_{n=1}^{N-1} \left(\sigma_n^\dagger \sigma_{n+1} + \sigma_{n+1}^\dagger \sigma_n \right) - h \sum_{n=1}^{N} \left(\tau_n^\dagger + \tau_n \right) + \text{h.c.}, \tag{21}$$

where J and h are the model parameters, σ_n and τ_n are local operators on each site defined as

$$\sigma_p = \left(\bigotimes_{q=1}^{p-1} I \right) \otimes \sigma \otimes \left(\bigotimes_{q=p+1}^{N} I \right) \tag{22}$$

and

$$\tau_p = \left(\bigotimes_{q=1}^{p-1} I \right) \otimes \tau \otimes \left(\bigotimes_{q=p+1}^{N} I \right), \tag{23}$$

with

$$\sigma = \begin{bmatrix} 1 & 0 & 0 & \cdots & 0 \\ 0 & \omega & 0 & \cdots & 0 \\ 0 & 0 & \omega^2 & \cdots & 0 \\ \vdots & \vdots & \vdots & \ddots & \vdots \\ 0 & 0 & 0 & \cdots & \omega^{k-1} \end{bmatrix}, \quad \tau = \begin{bmatrix} 0 & 0 & 0 & \cdots & 0 & 1 \\ 1 & 0 & 0 & \cdots & 0 & 0 \\ 0 & 1 & 0 & \cdots & 0 & 0 \\ 0 & 0 & 1 & \cdots & 0 & 0 \\ \vdots & \vdots & \vdots & \ddots & \vdots & \vdots \\ 0 & 0 & 0 & \cdots & 1 & 0 \end{bmatrix} \tag{24}$$

and $\omega = e^{2i\pi/k}$. These local operators satisfy $\sigma_n^k = \tau_n^k = I$ and $\sigma_n \tau_n = \omega \tau_n \sigma_n$, while they commute in different sites.

Then, we can apply Jordan-Wigner transformation, to introduce new operators

$$\alpha_{2p-1} = \sigma_p \prod_{q<p} \tau_q \tag{25}$$

and

$$\alpha_{2p} = -\omega \tau_p \sigma_p \prod_{q<p} \tau_q, \tag{26}$$

resulting in the Hamiltonian

$$H_{\text{clock}} = -J\omega \sum_{n=1}^{N-1} \alpha_{2n}^\dagger \alpha_{2n+1} - h\omega \sum_{n=1}^{N} \alpha_{2n-1}^\dagger \alpha_{2n} + \text{h.c.}. \tag{27}$$

These α_n operators are the so-called $\mathbb{Z}_k$ parafermions, and they satisfy position-dependent anticommutation relation

$$\alpha_p \alpha_q = \omega^{\text{sgn}(q-p)} \alpha_q \alpha_p, \tag{28}$$

while also satisfying

$$\alpha_n^k = I \quad \text{and} \quad \alpha_n^\dagger = \alpha_n^{k-1}. \tag{29}$$

In the fully dimerized limit $h = 0$ of the quantum clock model, two parafermionic operators α_1 and α_{2N} are not present, which means that we have a k-fold degeneracy in the system [40].

Note that in the case of $k = 2$, the parafermionic operators will be equivalent to the previously discussed Majorana fermions up to normalization and hence the clock model will be equivalent to the $w = \Delta$ Kitaev wire. The difference lies in the normalization conventions of the operators, and the phase convention of the model parameters. The other interesting case is when $k = 4$, as in this case, the degeneracy is fourfold, that is, it can be encoded in a half-spin fermion (i.e. an electron).

Let us conclude this section with some remarks regarding these exotic excitations. Majorana zero modes can be potentially realized in non-interacting systems, i.e. mean-field description is sufficient. With braiding alone, they can realize non-trivial unitary operators, but they cannot realize entangling qubit gates. Going further, $k > 2$ parafermions require interactions, i.e. mean-field description is not sufficient for treating them. However, even k parafermions can realize entangling gates with just braiding, and odd k parafermions promises universal quantum computation [41].

2.4 Bernevig–Hughes–Zhang model

In this subsection, we discuss some important consequences of time reversal symmetry concerning electron systems. Then, we introduce a topological insulator, the Bernevig-Huges-Zhang model, discuss its edge states and present the emergence of Majorana zero modes in it.

2.4.1 Consequences of time reversal symmetry

Wigner's theorem [42] guarantees that a symmetry transformation on (rays of) Hilbert spaces is representable by either a unitary or an antiunitary transformation on the same Hilbert spaces. The textbook example for the antiunitary symmetry is the time reversal symmetry $\mathscr{T}$, because it is important for a lot of physical systems, while being relatively easy to understand.

There are two, fundamentally different types of time reversal symmetries (TRS): $\mathscr{T}^2 = 1$, which is called bosonic TRS, and $\mathscr{T}^2 = -1$, which is called fermionic TRS. This is because for any state ψ, we have that (where the $\pm$ stands for the sign of $\mathscr{T}^2$)

$$(\mathscr{T}\psi|\psi) = (\mathscr{T}^2\psi|\mathscr{T}\psi)^* = (\pm\psi|\mathscr{T}\psi)^* = \pm(\mathscr{T}\psi|\psi). \tag{30}$$

Bosonic TRS has no physically important consequence, but when $\mathscr{T}^2 = -1$, it gives us Kramers' Degeneracy: $(\mathscr{T}\psi|\psi) = 0$, i.e. $\mathscr{T}\psi$ and ψ are orthogonal. This is especially important when ψ is an eigenvector of the Hamiltonian, because then $\mathscr{T}\psi$ will be another eigenvector with the same energy, implying at least twofold degeneracy for all eigenvalues in the spectrum.

From a given Hamiltonian H, there is a simple way to create a new Hamiltonian that has bosonic or fermionic TRS, by "doubling the Hilbert space". That is, we take a copy if the system, conjugate it, and couple the two systems by an operator C, so the Hamiltonian will be

$$H_{\mathrm{TRI}} = \begin{bmatrix} H & C \\ C^\dagger & H^* \end{bmatrix}. \tag{31}$$

Depending on C, our new Hamiltonian H_{TRI} can have bosonic or fermionic TRS:. If C is symmetric, i.e. $C = C^t$, we will have a bosonic TRS with $\mathscr{T} = \sigma_x \otimes IK$, and if C is anti-symmetric, i.e. $C = -C^t$, we will have a fermionic TRS with $\mathscr{T} = i\sigma_y \otimes IK$, where I is the identity operator on the original Hilbert space.

2.4.2 Bernevig–Hughes–Zhang Hamiltonian

The BHZ model, which is a topological insulator [7], can be constructed from the TRS-breaking Qi-Wu-Zhang (QWZ) model [7, 43] by the previously mentioned "doubling the Hilbert space" method. There is a huge freedom in the choice of the coupling C that makes it possible to generate a broad range of models, but we are sticking with $C = 0$. The QWZ model is a Chern insulator with topologically protected edge states, but as it breaks the TRS, they are not Kramers pairs. However the newly introduced doubled BHZ model will have edge states that are TRS partners.

The Hamiltonian of the model, on rectangular $N_x \times N_y$ grid, is

$$
\begin{aligned}
H_{\mathrm{BHZ}} = u \sum_{m_x=1}^{N_x} \sum_{m_y=1}^{N_y} c^\dagger_{m_x,m_y} \begin{bmatrix} \sigma_y & 0 \\ 0 & \sigma_y^* \end{bmatrix} c_{m_x,m_y} \\
+ \frac{1}{2} \sum_{m_x=1}^{N_x-1} \sum_{m_y=1}^{N_y} c^\dagger_{m_x+1,m_y} \begin{bmatrix} \sigma_y + i\sigma_x & 0 \\ 0 & (\sigma_y + i\sigma_x)^* \end{bmatrix} c_{m_x,m_y} + \mathrm{h.c.} \\
+ \frac{1}{2} \sum_{m_x=1}^{N_x} \sum_{m_y=1}^{N_y-1} c^\dagger_{m_x,m_y+1} \begin{bmatrix} \sigma_y + i\sigma_z & 0 \\ 0 & (\sigma_y + i\sigma_z)^* \end{bmatrix} c_{m_x,m_y} + \mathrm{h.c.}
\end{aligned}
\tag{32}
$$

where u is the so-called sublattice parameter and σ_i are the Pauli-matrices acting on the orbital degree of freedom (with possible values p_+ and p_-), the conjugation of the matrices are meant element-wise, and

$$
c_{m_x,m_y} = \begin{bmatrix} c_{m_x,m_y,\uparrow,p_+} \\ c_{m_x,m_y,\uparrow,p_-} \\ c_{m_x,m_y,\downarrow,p_+} \\ c_{m_x,m_y,\downarrow,p_-} \end{bmatrix}. \tag{33}
$$

Note that this system has $\mathscr{T}^2 = -1$ TRS symmetry, which gives rise to topologically protected edge states [7, 44].

For the ease of readability, we introduce different notation for the Pauli-matrices acting on the spin and orbital degree of freedom. From now on, we will keep the σ_i notation for the orbital degree of freedom, while we will denote them with s_i if they are acting on the spin degree of freedom.

2.4.3 Edge states in the BHZ model

The observed topological invariant of the model is the parity of the number of edge state Kramers pairs on a terminated part of an edge [7, 44]. This invariant is usually called the $\mathbb{Z}_2$-invariant, and I will denote it as D. This $\mathbb{Z}_2$-invariant is invariant in the sense that it cannot change due to adiabatic deformation of the Hamiltonian (continuous change, that respects the TRS and does not close the bulk gap). Depending on the value of D, we can have either a trivial insulator ($D = 0$) or a topological insulator ($D = 1$), and the transition between them can be achieved by tuning the sublattice parameter u. The topologically interesting situation is when $D = 1$: in this case, at least one edge state

Kramers pair is topologically protected against disorder, and it turns out that it will also be perfectly transmitting [7].

In Figure 3, besides the electron density profile of a typical edge state (top left) and bulk state (top right), we also show the complete spectrum with the $E \approx 0$ part emphasized (bottom) for a "potato-shaped" BHZ sample with $u = -1$. We find that the edge state is, in fact, concentrated at the edge of the sample, while the bulk state has a considerable weight on all sites. The whole spectrum is degenerate due to TRS, as we expected. This degeneracy can also be seen for the $E \approx 0$ region in the figure.

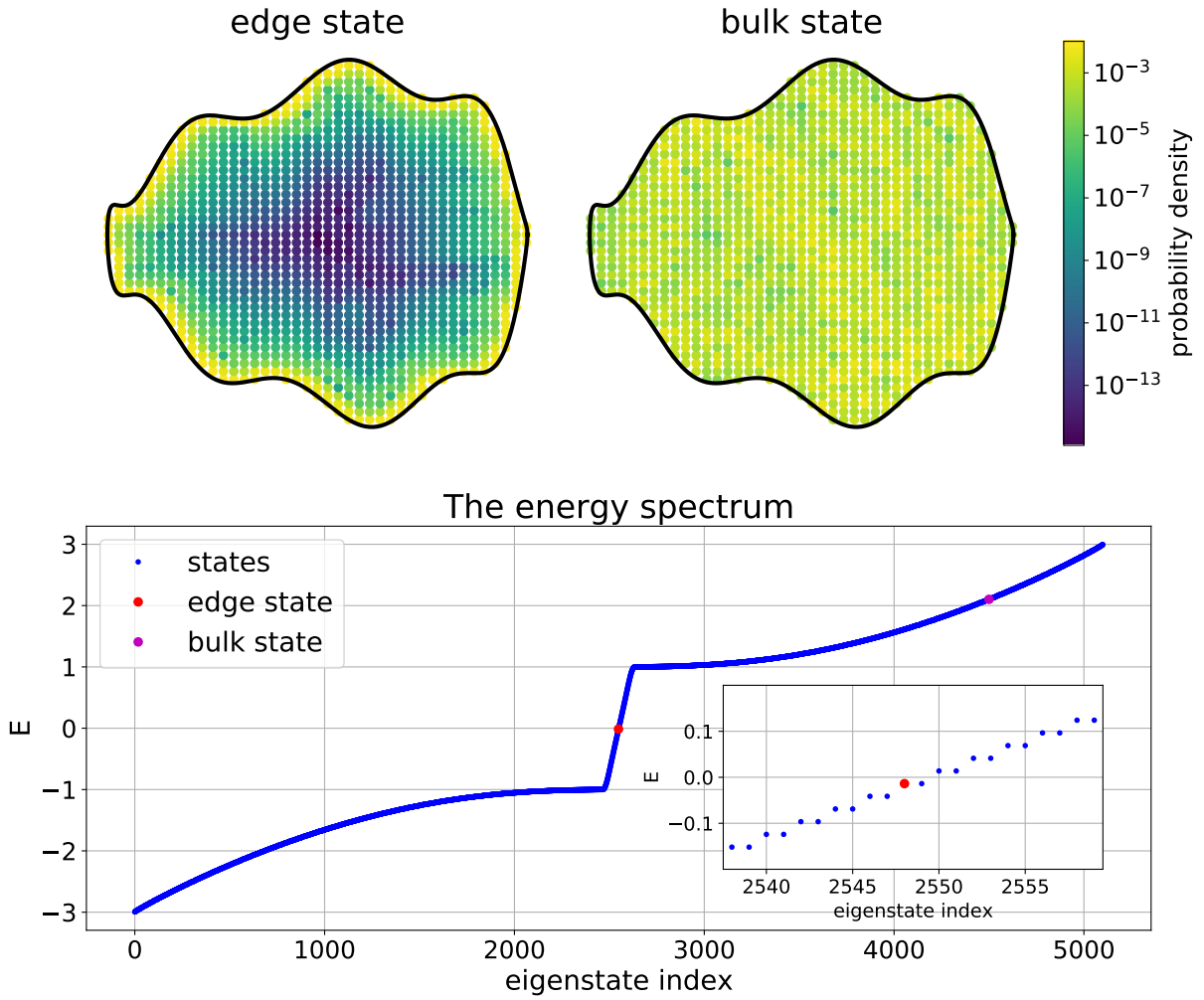

Figure 3: The absolute value square of the wave function of an edge state of the "potato-shaped" BHZ sample with $u = -1$, as a function of the lattice index.

In Figure 4, we see the Local Density Of States (LDOS) of the "potato-shaped" BHZ sample, calculated by the Kernel Polynomial Method (KPM), which approximates the LDOS of the Hamiltonian using its Chebysev expansion [45]. It can be seen that the spectrum of the bulk has a well-defined energy gap, while on the edge of the sample there is considerable spectral weight associated to the energy range coinciding with the bulk gap.

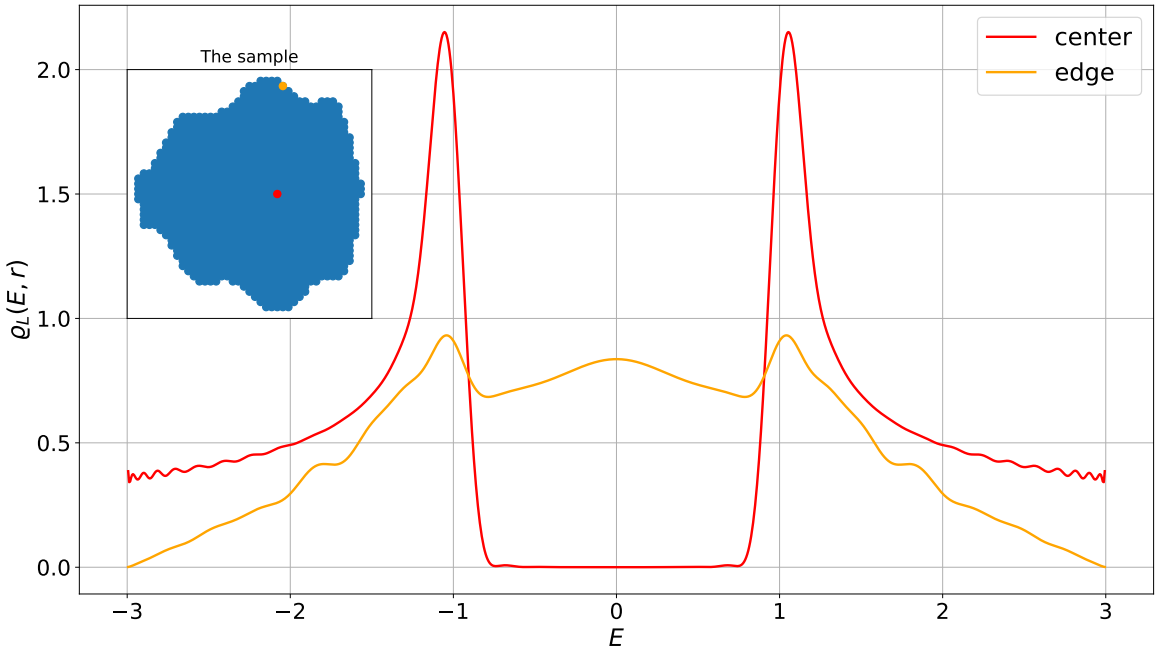

Figure 4: The local density of states of the "potato-shaped" BHZ model with $u = -1$ at sampled in two representative coordinates, i.e. at the edge and in the center of the model.

In order to understand the nature of the edge states better, we consider now the spectrum of an infinite BHZ stripe (infinite in the y-direction) and examine its dispersion relation. If we set $u = -1$ again and add an extra "shift term" to the Hamiltonian in the form of

$$H_{\text{shift}} = V \sum_{m_y} \left(c^\dagger_{1,m_y} I c_{1,m_y} - c^\dagger_{N_x,m_y} I c_{N_x,m_y} \right) \tag{34}$$

for a small constant V and 4×4 identity matrix $I = s_0 \otimes \sigma_0$, we will shift the energies at the left edge "up", and at the right edge "down". This is useful for us, because it makes clear the fact that there are 4 edge states overall: 2 located exponentially on the left side of the stripe, and 2 on the right, as can be seen in Figure 5.

Note that we have been using real space lattice Hamiltonians, but for translationally invariant systems, where the wavenumber k is a good quantum number (like in the case of our stripe, where it's translationally invariant in the y direction), we can Fourier transform the Hamiltonian to get the bulk momentum-space Hamiltonian $H(k)$. In Figure 5, the dispersion relation of the transformed system is the k_y-dependent spectrum of the transformed Hamiltonian $H(k_y)$.

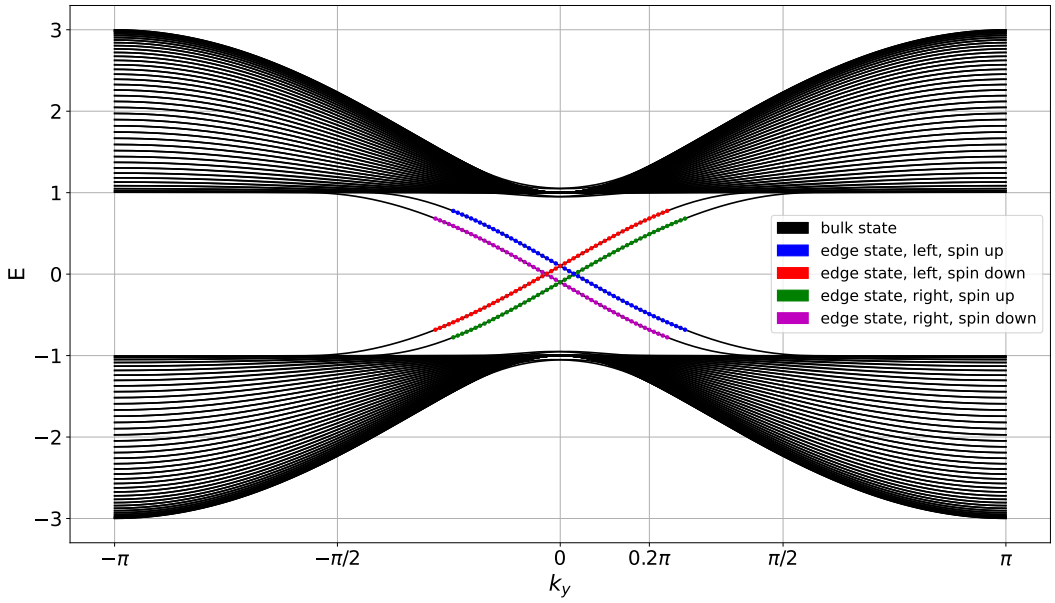

Figure 5: The dispersion relation of a BHZ stripe with $u = -1$, width $N_x = 40$ and "shift parameter" $V = 0.1$. A state is marked as "edge state" if it has more than 90% weight on the 3 left-most or right-most states.

A widely used tool for translationally invariant lattice models is the so-called envelope function approximation (EFA), which provides a rigorous continuum approximation for a lattice Hamiltonian around a given momentum k_0 [7]. The method consist of expanding the original bulk momentum-space Hamiltonian $H(k)$ around k_0, and in the expansion replacing $k - k_0$ by the momentum (differential) operator p.

Figure 5 also shows the general property of the effective low energy Hamiltonian of the edge states: it is linear in the momentum k_y and is proportional to s_z. Looking at the left and right sides, we see that they have opposite group velocities. This means that the EFA of the edge states around $k_y = 0$ (up to linear order) should be in the form of

$$H_{\text{BHZ edge, 1}}(p) \propto p s_z \otimes \zeta_z, \tag{35}$$

where we introduced the ζ_i notation for the Pauli-matrices acting on the "side" degree of freedom.

Figure 5 could imply mixing between those four edge states at a given energy (as it would not violate the energy conservation), deep inside the bulk gap, due to, for example, defect in the system. However this is not possible. The edge states are exponentially localized at the edges, which is shown in Figure 6 for $k_x = 0.2\pi$, hence crossing between left and right edge states is not possible (if the sample is wide enough). However, the two edge states on the same edge are not separated spatially, but are protected by the TRS.

These localized band of Kramers-pair states are one of the key building blocks in the Majorana [23] and parafermion platforms [35,39]. In the Majorana platforms they provide an effective Fermi surface where spin degeneracy is lifted which is needed for effective topological p-wave superconductivity to arise once the sample is proximitized with an s-wave superconductor. For parafermion platforms, using time reversal invariance of this system, in conjunction with strong interactions leads potentially to the required fourfold degenerate ground state.

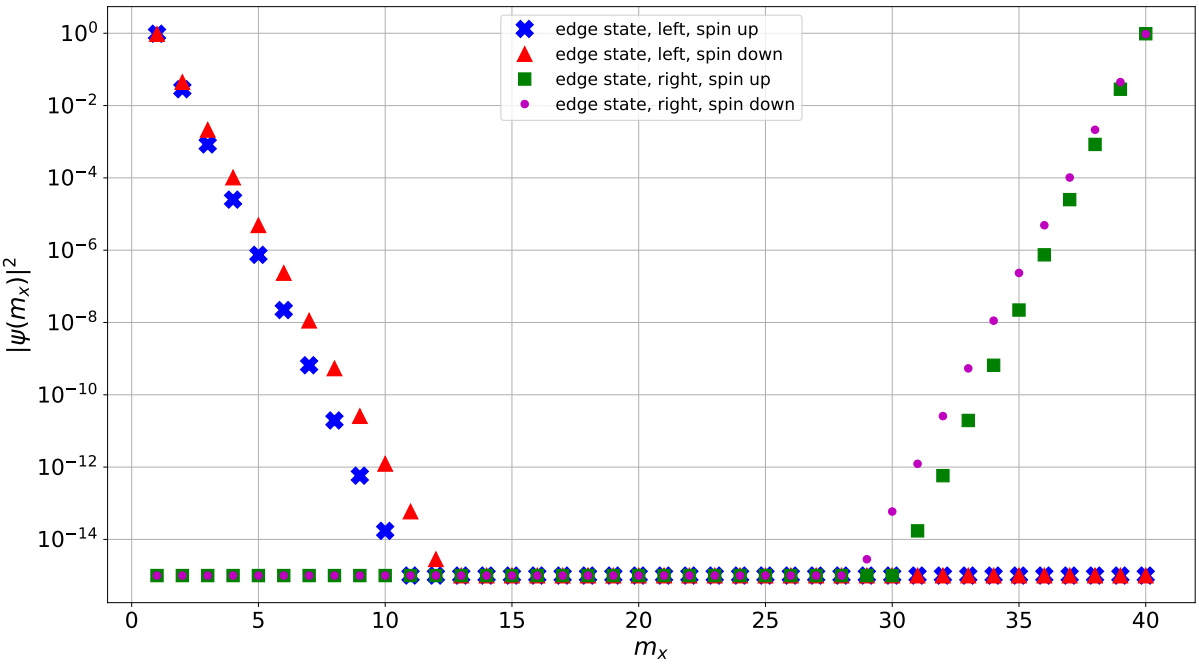

Figure 6: The probability density of the edge states of a BHZ stripe with $u = -1$, width $N_x = 40$ and "shift parameter" $V = 0.1$, at $k_y = 0.2\pi$.

2.4.4 Majorana zero modes in the BHZ model

To observe Majorana Zero Modes in the BHZ model, we can simply add magnetic field and superconductivity to it. The site-specific magnetic field

$$B(m_x, m_y) = [B_x(m_x, m_y), B_y(m_x, m_y), B_z(m_x, m_y)] \tag{36}$$

can be added to the model with the Hamiltonian

$$H_{\mathrm{B}} = \sum_{m_x, m_y} c^{\dagger}_{m_x, m_y} \big(B(m_x, m_y) \cdot s\big) \otimes \sigma_0 c_{m_x, m_y}, \tag{37}$$

where s is the vector of Pauli-matrices acting on the spin degree of freedom.

The site-specific superconductivity $\Delta(m_x, m_y)$ has the form

$$H_{\mathrm{sc}} = \frac{1}{2} \sum_{m_x, m_y} \Delta(m_x, m_y) c^{\dagger}_{m_x, m_y} \begin{bmatrix} 0 & \sigma_0 \\ -\sigma_0 & 0 \end{bmatrix} c^{\dagger}_{m_x, m_y} + \mathrm{h.c.}. \tag{38}$$

Therefore, in the following we solve extended Hamiltonian $H_{\mathrm{BHZ}} + H_{\mathrm{B}} + H_{\mathrm{sc}}$ by the BdG transformation. Note that the magnetic field and superconductivity are position-dependent in the sense that they both have a non-zero value in a given region, and zero in its complementer. Because of this, we can characterise them with a vector and a number respectively, alongside their supports. In Figure 7 we consider the same potato geometry as in Figure 3, but we apply additional superconductivity and magnetic field in separate halves of the system. Here, color blue and red encodes lattice sites where $B = [0.2, 0, 0]$ external magnetic field was applied and $\Delta = 0.2$ superconductivity was assumed, respectively.

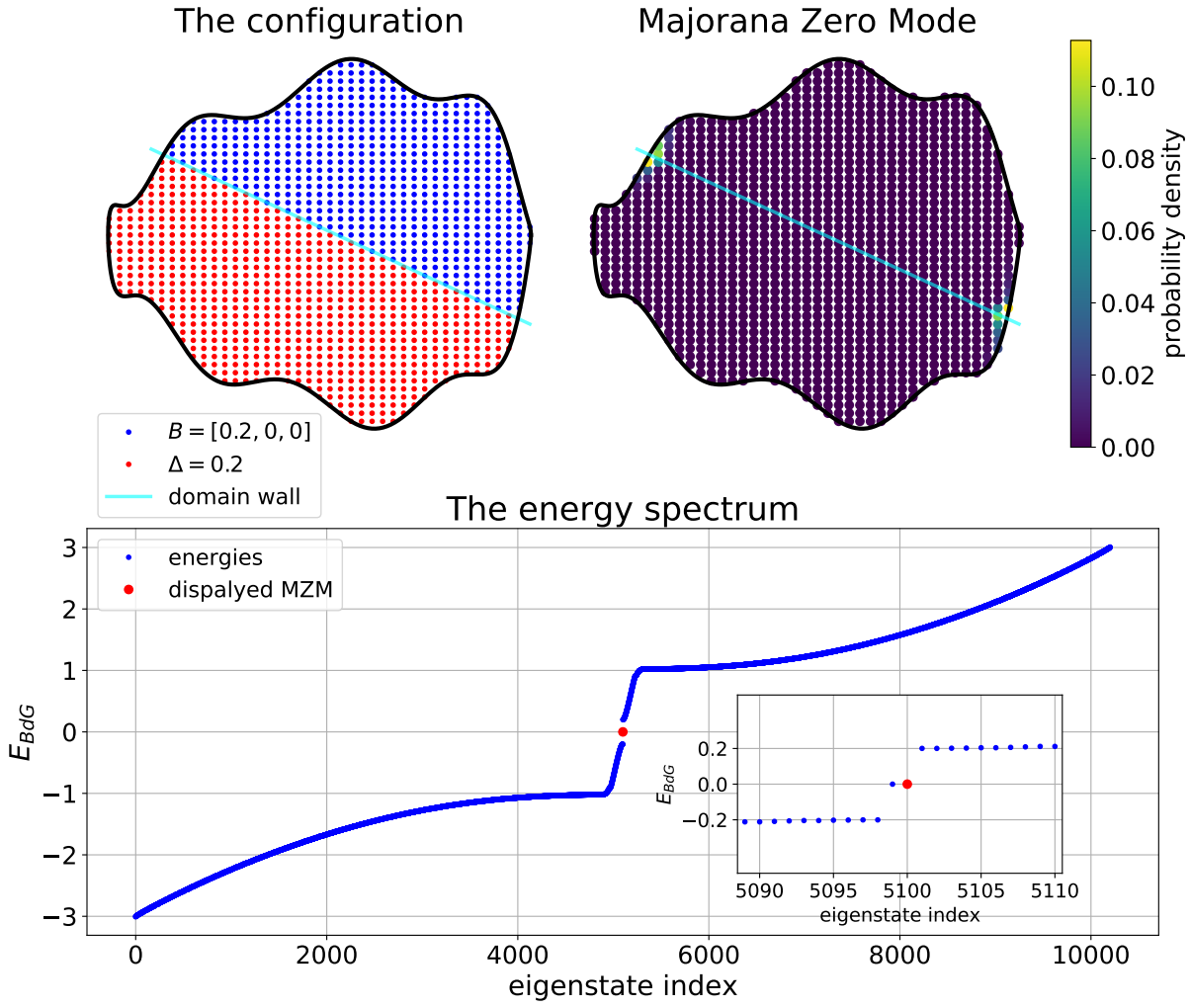

Figure 7: The "potato-shaped" BHZ model with $u = -1$, with magnetic field and superconductivity.

In agreement with literature results [23, 25], we identify Majorana zero modes which localize at the border of the superconducting and magnetic regimes of the edge of the sample. Even though MZMs might be constructed in such setup theoretically, its experimental realization is an extraordinary challenge as the magnetic field can suppress the superconductivity.

Alternatively, instead of the magnetic field, TRS preserving interactions [35, 39] can also be applied to open a gap in the subsystem which complements the superconducting half of the sample. But to do that, the BdG method cannot be used as interaction terms are not quadratic in the creation and annihilation operators. To treat such more general problems, in the following, we use the density matrix renormalization group method which excels in studying low-dimensional interacting quantum systems [46].

3 Density-matrix renormalization group algorithm

The density-matrix renormalization group algorithm (DMRG) is a numerical variational technique, specialized to obtain the low-energy physics of quantum many-body systems. It was first developed by Steven R. White [46], to solve the problem of a particle in a one-dimensional box (which is a simple problem analytically, but all of the previous Renormalization Group methods failed to solve it).

In the following we present the theory of the DMRG method, but first we need to discuss some important tools and definitions. In this section, we will try to stick the notations used in [47]. Note that in the following subsections, we will work with open boundary conditions, as this is the one being used most of the time for the DMRG calculations. However, there is a special form for periodic boundary condition, which can be found in [47] as well.

In our project we used the Budapest-DMRG [48] package for preliminary studies and benchmarking, and the ITensor implementation of DMRG [49] for production calculations. These codes can treat general models, the actual Hamiltonian to be investigated are to be constructed by the user.

3.1 Singular value decomposition

One of the key mathematical tools of the DMRG method is the singular value decomposition (SVD). If M is an $m \times n$ complex or real matrix, then it can be written as

$$M = USV^{\dagger}, \tag{39}$$

where U is an $m \times m$ complex unitary matrix, V is an $n \times n$ complex unitary matrix and S is an $m \times n$ rectangular diagonal matrix with non-negative numbers on the diagonal. The diagonal entries of the S matrix are called the singular values of M, and are usually denoted by $s_i = S_{i,i}$. The number of non-zero singular values are equal to the rank of the matrix M, and it is usually denoted by r. The columns of U (the so-called left-singular vectors of M), denoted as $u_1, \ldots, u_m$; and the columns of V (the so-called right-singular values of M), denoted as $v_1, \ldots, v_n$, form two set of orthonormal bases, and with them,

we can rewrite (39) as

$$M = \sum_{i=1}^{r} s_i u_i v_i^\dagger. \tag{40}$$

Let us assume that the singular values $\{s_i\}_{i=1}^r$ are in decreasing order. Then, this form is really useful for approximations: Eckart–Young–Mirsky theorem [50] states that the "best" rank $r' \leqslant r$ approximation of the matrix M is

$$M' = \sum_{i=1}^{r'} s_i u_i v_i^\dagger, \tag{41}$$

where the "best" means that M' is the closest rank r' matrix to M in both the (induced) 2-norm $\|.\|_2$, defined as

$$\|M\|_2 = \sup_{\|v\|_2=1} \|Mv\|_2, \tag{42}$$

and in the Frobenius norm $\|.\|_{\mathrm{F}}$, defined as

$$\|M\|_{\mathrm{F}} = \sqrt{\sum_{i=1}^{m}\sum_{j=1}^{n} |M_{ij}|^2} = \sqrt{\mathrm{Tr}\,(M^\dagger M)}. \tag{43}$$

However, these norms have a much simpler form using the singular values of the matrix M:

$$\|M\|_2 = \max_i\{s_i\} = s_1, \tag{44}$$

and

$$\|M\|_{\mathrm{F}} = \sqrt{\sum_{i=1}^{r} s_i^2}. \tag{45}$$

The SVD decomposition of a given matrix M can by attained by solving the eigen-problem of both $MM^\dagger$ and $M^\dagger M$: the left-singular vectors of M can be chosen as a set of orthonormal eigenvectors of $MM^\dagger$; similarly, the right-singular vectors of M can be chosen as a set of orthonormal eigenvectors of $M^\dagger M$; and finally the non-zero singular values of M are the square roots of the non-zero eigenvalues of both $MM^\dagger$ and $M^\dagger M$.

Up to this point, everything was just pure mathematics, without any obvious relevance in modelling physical problems. To see its importance, let us assume that our physical system is partitioned into 2 parts, A with dimension N_A and B with dimension N_B. Then, given a pure state $|\psi\rangle$, and orthonormal bases for A as $\{|i\rangle_A\}_i$ and for B as $\{|j\rangle_B\}_j$, we can decompose $|\psi\rangle$ as

$$|\psi\rangle = \sum_{i,j} \Psi_{i,j} |i\rangle_A |j\rangle_B. \tag{46}$$

This form gives a short formula for the reduced density matrices:

$$\rho_A = \mathrm{Tr}_B \, |\psi\rangle\langle\psi| = \Psi\Psi^\dagger \tag{47}$$

and

$$\rho_B = \mathrm{Tr}_A \, |\psi\rangle\langle\psi| = \Psi^\dagger\Psi. \tag{48}$$

We can also carry out the SVD on the matrix Ψ, to obtain

$$\begin{aligned} |\psi\rangle &= \sum_{i,j} \sum_{a=1}^{\min(N_A,N_B)} U_{i,a} S_{a,a} V^*_{j,a} |i\rangle_A |j\rangle_B \\ &= \sum_{a=1}^{\min(N_A,N_B)} \Big(\sum_i U_{i,a} |i\rangle_A \Big) s_a \Big(\sum_j V^*_{j,a} |j\rangle_B \Big). \end{aligned} \tag{49}$$

From this, we can define a new set of orthonormal (because U and $V^\dagger$ are orthonormal) states on both A and B as

$$|a\rangle_A = \sum_i U_{i,a} |i\rangle_A \tag{50}$$

and

$$|a\rangle_B = \sum_j V^*_{j,a} |j\rangle_B, \tag{51}$$

to reach the much simpler form

$$|\psi\rangle = \sum_{a=1}^{\min(N_A,N_B)} s_a |a\rangle_A |a\rangle_B. \tag{52}$$

However, some of the singular values can be zero, resulting in even fewer terms. Thanks to ordering the singular values in decreasing order, it means that we need to sum up only the first $r \leqslant \min(N_A, N_B)$ terms, where r is the rank of the original matrix. This way, we achieved the so-called Schmidt decomposition

$$|\psi\rangle = \sum_{a=1}^{r} s_a |a\rangle_A |a\rangle_B, \tag{53}$$

where $r = 1$ corresponds to classical product states, and $r > 1$ corresponds to entangled quantum states.

From this form, we can carry out the partial traces easily, to reach

$$\rho_A = \sum_{a=1}^{r} s_a^2 |a\rangle_{AA}\langle a| \tag{54}$$

and

$$\rho_B = \sum_{a=1}^{r} s_a^2 |a\rangle_{BB}\langle a|, \tag{55}$$

showing that they have the same non-zero eigenvalues, with different eigenvectors. This simple form will even be present if we were to approximate ψ, since the 2-norm of ψ is equal to the Frobenius norm of the matrix Ψ. This means that (thanks to the SVD) the best rank r' approximation Ψ' of Ψ will provide the best approximation ψ' for ψ as well. With this approximate state, we could repeat the whole calculation to reach its Schmidt decomposition

$$|\psi'\rangle = \sum_{a=1}^{r'} \sigma_a |a\rangle_A |a\rangle_B. \tag{56}$$

3.2 Matrix product states

Let us assume that we have L sites, each with a d-dimensional local state space $\{\sigma_i\}_{i=1}^{d}$. Then, the most general pure quantum state can be written as

$$|\psi\rangle = \sum_{\sigma_1,\ldots,\sigma_L} c_{\sigma_1,\ldots,\sigma_N} |\sigma_1,\ldots,\sigma_N\rangle. \tag{57}$$

In fact, the $c_{\sigma_1,\ldots,\sigma_N}$ tensor of coefficients can be equivalently rewritten in a special form of product of matrices which representation is called matrix product state (MPS) [51]. That is, we can write it as

$$c_{\sigma_1,\ldots,\sigma_N} = M^{\sigma_1}\cdots M^{\sigma_N}, \tag{58}$$

where M^{σ_i} are matrices, that can have different shapes (but they need to have shapes "compatible" with the matrix multiplication). Note that the first (M^{σ_1}) and last (M^{σ_N}) matrices are row and column matrices respectively (this is required so that the result of the multiplication is a scalar).

For the DMRG calculations, we regularly bipartion our system into A and B, with sites $1, \ldots, l$ being in A and $l+1, \ldots, L$ in B. For these scenarios, we introduce new basis states

$$|a_l\rangle_A = \sum_{\sigma_1,\ldots,\sigma_l} \left(M^{\sigma_1} \cdots M^{\sigma_l}\right)_{1,a_l} |\sigma_1, \ldots, \sigma_l\rangle \tag{59}$$

and

$$|a_l\rangle_B = \sum_{\sigma_{l+1},\ldots,\sigma_L} \left(M^{\sigma_{l+1}} \cdots M^{\sigma_L}\right)_{a_l,1} |\sigma_{l+1}, \ldots, \sigma_L\rangle. \tag{60}$$

Using these states, the MPS becomes

$$|\psi\rangle = \sum_{a_l} |a_l\rangle_A |a_l\rangle_B. \tag{61}$$

A Matrix Product State can be represented graphically as well, with the so-called tensor diagram notation [52]. In Figure 8, we see the tensor diagram of an open boundary condition MPS state, with $N = 5$.

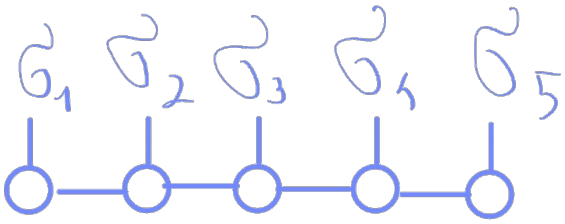

Figure 8: The tensor diagram of a Matrix Product State with $N = 5$ and open boundary conditions.

Every state of the form of (57) can be represented in an MPS form (with big enough matrices), but this representation is not unique. There are several ways of construction detailed in the article [47] using Singular Value Decompositions (SVD) repeatedly on the coefficients $c_{\sigma_1,\ldots,\sigma_N}$.

The so-called left-canonical matrix product state can be constructed by first doing an SVD on the matrix $\Psi_{\sigma_1,(\sigma_2,\ldots,\sigma_N)} = c_{\sigma_1,\ldots,\sigma_N}$, which gives

$$\Psi_{\sigma_1,(\sigma_2,\ldots,\sigma_N)} = \sum_{a_1=1}^{r_1} U_{\sigma_1,a_1} S_{a_1,a_1} \left(V^\dagger\right)_{a_1,(\sigma_2,\ldots,\sigma_N)}. \tag{62}$$

Then, we can denote U_{σ_1,a_1} as $A^{\sigma_1}_{a_1}$ and $S_{a_1,a_1}\left(V^\dagger\right)_{a_1,(\sigma_2,\ldots,\sigma_N)}$ as $c_{a_1,\sigma_2,\ldots,\sigma_L}$ to get

$$c_{\sigma_1,\ldots,\sigma_L} = \sum_{a_1=1}^{r_1} A^{\sigma_l}_{a_1} c_{a_1,\sigma_2,\ldots,\sigma_L}. \tag{63}$$

Again, we form a matrix $\Psi_{(a_1,\sigma_2),(\sigma_3,\ldots,\sigma_N)} = c_{a_1,\sigma_2,\ldots,\sigma_N}$, and decompose it as

$$\Psi_{(a_1,\sigma_2),(\sigma_3,\ldots,\sigma_N)} = \sum_{a_2=1}^{r_2} U_{(a_1,\sigma_2),a_2} S_{a_2,a_2}\left(V^\dagger\right)_{a_2,(\sigma_3,\ldots,\sigma_N)}. \tag{64}$$

Similarly to before, we can denote $U_{(a_1,\sigma_2),a_1}$ as $A^{\sigma_2}_{a_1,a_2}$ and $S_{a_2,a_2}\left(V^\dagger\right)_{a_2,(\sigma_3,\ldots,\sigma_N)}$ as $c_{a_2,\sigma_3,\ldots,\sigma_L}$ to reach

$$c_{\sigma_1,\ldots,\sigma_L} = \sum_{a_1=1}^{r_1}\sum_{a_2=1}^{r_2} A^{\sigma_l}_{a_1} A^{\sigma_2}_{a_1,a_2} c_{a_2,\sigma_3,\ldots,\sigma_L}. \tag{65}$$

Continuing this procedure, we will get

$$c_{\sigma_1,\ldots,\sigma_N} = \sum_{a_1,\ldots,a_{L-1}} A^{\sigma_1}_{a_1} A^{\sigma_2}_{a_1,a_2} \cdots A^{\sigma_{L-1}}_{a_{L-2},a_{L-1}} A^{\sigma_L}_{a_{L-1}} = A^{\sigma_1}\cdots A^{\sigma_L}. \tag{66}$$

These A^{σ_i} matrices are left-normalized, which means that

$$\sum_{\sigma_i} A^{\sigma_i\dagger} A^{\sigma_i} = I. \tag{67}$$

The right-canonical matrix product state is constructed the same way, except instead of going from left to right, we we proceed in the reversed order. The result will be similar to (66):

$$c_{\sigma_1,\ldots,\sigma_N} = B^{\sigma_1}\cdots B^{\sigma_L}, \tag{68}$$

but they will be right-normalized instead,

$$\sum_{\sigma_i} B^{\sigma_i} B^{\sigma_i\dagger} = I. \tag{69}$$

Notice that we used the letter A for left-normalized matrices, and B for right-normalized matrixes. This is just a convention, to make some calculations easier to follow. We can mix the previous two decomposition as well, to achieve the so-called mixed-canonical matrix product state. During the construction, we do the left-canonical decomposition of $c_{\sigma_1,\ldots,\sigma_N}$ up to the index l:

$$c_{\sigma_1,\ldots,\sigma_N} = \sum_{a_l} \left(A^{\sigma_1}\cdots A^{\sigma_l}\right)_{a_l} S_{a_l,a_l}\left(V^\dagger\right)_{a_l,(\sigma_{l+1},\ldots,\sigma_L)}, \tag{70}$$

and after this, we do the right-canonical decomposition on $\left(V^{\dagger}\right)_{a_l,(\sigma_{l+1},\ldots,\sigma_L)}$ to reach

$$\begin{aligned} c_{\sigma_1,\ldots,\sigma_N} &= \sum_{a_l} \left(A^{\sigma_1}\cdots A^{\sigma_l}\right)_{a_l} S_{a_l,a_l} \left(B^{\sigma_{l+1}}\cdots B^{\sigma_l}\right)_{a_l} \\ &= A^{\sigma_1}\cdots A^{\sigma_l} S B^{\sigma_{l+1}}\cdots B^{\sigma_l}. \end{aligned} \tag{71}$$

Note that S is the matrix containing the singular values of the site l and in this case, the A^{σ_i} matrixes are left-normalized, while the B^{σ_i} matrices are right-normalized. In Figure 9 we see the tensor diagram of mixed-canonical MPS with $N = 5$ and $l = 3$.

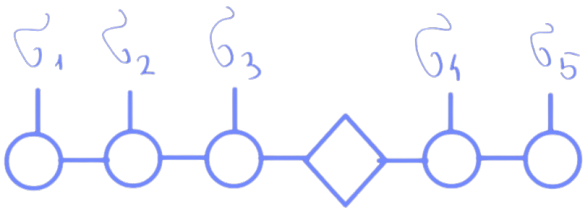

Figure 9: The mixed-canonical matrix product state with $N = 5$ and $l = 3$.

We've seen 3 different way of constructing an MPS from a given state, and all of them are different. But even from a given set of matrices M^{σ_i} (which can be one of the previous 3 constructions or a totally different one), we can construct a new one by gauge transformation. Let us pick two adjacent sets of matrices: M^{σ_j} and $M^{\sigma_{j+1}}$. Their dimensions, in general, can be written as $d_1 \times D$ and $D \times d_2$. If we pick an invertible $D \times D$ matrix X, we can transform the M matrices as

$$M^{\sigma_j} \mapsto M^{\sigma_j} X \quad \text{and} \quad M^{\sigma_{j+1}} \mapsto X^{-1} M^{\sigma_{j+1}}. \tag{72}$$

In the article [47], there are several methods and properties derived, however, I would like to emphasize only two of them: the inner product of two vectors and the reduced density operators.

Given two states ψ and ϕ, which are represented by the matrices M^{σ_i} and N^{σ_i} respectively, their inner product is simply

$$\langle\phi|\psi\rangle = \sum_{\sigma_1,\ldots,\sigma_L} \left(N^{\sigma_L}\right)^{\dagger}\cdots\left(N^{\sigma_1}\right)^{\dagger} M^{\sigma_1}\cdots M^{\sigma_L}. \tag{73}$$

In Figure 10, we see the tensor diagram of the product of two MPSs with $N = 5$. Note that they do not have any "legs" left, symbolizing that the result is a scalar.

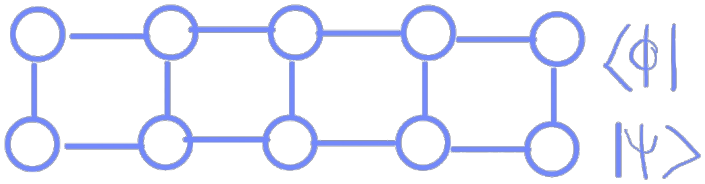

Figure 10: The tensor diagram of the inner product of two Matrix Product States with $N = 5$.

In the special case, when $\phi = \psi$, we can rewrite (73) as

$$\langle\psi|\psi\rangle = \sum_{\sigma_l} \sum_{a_{l-1},a_l} \sum_{a'_{l-1},a'_l} \Psi^A_{a_{l-1},a'_{l-1}} M^{\sigma_l *}_{a_{l-1},a_l} M^{\sigma_l}_{a'_{l-1},a'_l} \Psi^B_{a_l,a'_l}, \tag{74}$$

where l is an arbitrary site,

$$\Psi^A_{a_{l-1},a'_{l-1}} = \sum_{\sigma_1,\ldots,\sigma_{l-1}} \left(M^{\sigma_{l-1}\dagger} \cdots M^{\sigma_l\dagger} M^{\sigma_1} \cdots M^{\sigma_{l-1}}\right)_{a_{l-1},a'_{l-1}} \tag{75}$$

and

$$\Psi^B_{a_l,a'_l} = \sum_{\sigma_{l+1},\ldots,\sigma_L} \left(M^{\sigma_{l+1}} \cdots M^{\sigma_L} M^{\sigma_L\dagger} \cdots M^{\sigma_{l+1}\dagger}\right)_{a'_l,a_l}. \tag{76}$$

This form, at the current point, might look more complicated than the initial one, but in the special case, when the sites $1,\ldots,l-1$ are left-normalized and sites $l+1,\ldots,L$ are right-normalized, it becomes much simpler, as

$$\Psi^A_{a_{l-1},a'_{l-1}} = \delta_{a_{l-1},a'_{l-1}} \quad \text{and} \quad \Psi^B_{a_l,a'_l} = \delta_{a_l,a'_l}. \tag{77}$$

If the system is split into A ($i = 1,\ldots,l$) and B ($i = l+i,\ldots,L$) parts as before, the reduced density operators are defined as the partial trace of the projector of the state

$$\psi = \sum_{\sigma} M^{\sigma_1} \cdots M^{\sigma_L} |\sigma\rangle, \tag{78}$$

i.e.

$$\rho^{[l]}_A = \mathrm{Tr}_B\, |\psi\rangle\langle\psi| = \sum_{\sigma,\sigma'\in A} M^{\sigma_1} \cdots M^{\sigma_l} \varrho^{[l]}_A M^{\sigma'_l\dagger} \cdots M^{\sigma'_1\dagger} |\sigma\rangle\langle\sigma'| \tag{79}$$

and

$$\rho^{[l]}_B = \mathrm{Tr}_A\, |\psi\rangle\langle\psi| = \sum_{\sigma,\sigma'\in B} M^{\sigma'_L\dagger} \cdots M^{\sigma'_{l+1}\dagger} \varrho^{[l]}_B M^{\sigma_{l+1}\dagger} \cdots M^{\sigma_L\dagger} |\sigma\rangle\langle\sigma'|, \tag{80}$$

where σ is just the vector of σ_is (i.e. $(\sigma)_i = \sigma_i$) and $\varrho_A^{[l]}$ and $\varrho_B^{[l]}$ satisfy the

$$\varrho_A^{[l-1]} = \sum_{\sigma_l} M^{\sigma_l} \varrho_A^{[l]} M^{\sigma_l \dagger} \tag{81}$$

and

$$\varrho_B^{[l]} = \sum_{\sigma_l} M^{\sigma_l \dagger} \varrho_B^{[l-1]} M^{\sigma_l} \tag{82}$$

recursive relations. These formulas can be further simplified when the MPS is normalized in a given way. When it is a mixed canonical state

$$\psi = \sum_{\sigma} A^{\sigma_1} \cdots A^{\sigma_{l-1}} \Psi^{\sigma_l} B^{\sigma_{l+1}} \cdots B^{\sigma_L} |\sigma\rangle, \tag{83}$$

we simply have

$$\rho_A^{[l]} = \Psi \Psi^\dagger \quad \text{and} \quad \rho_B^{[l]} = \Psi^\dagger \Psi. \tag{84}$$

3.3 Matrix product operators

Along the same lines as in the previous subsection, we can define a special form of operators: the matrix product operators (MPO). A general operator H can be written as

$$H = \sum_{\sigma_1,\ldots,\sigma_N,\sigma'_1,\ldots,\sigma'_N} c_{\sigma_1,\ldots,\sigma_N;\sigma'_1,\ldots,\sigma'_N} |\sigma_1,\ldots,\sigma_N\rangle\langle\sigma'_1,\ldots,\sigma'_N|, \tag{85}$$

and in this case, we call the operator a Matrix Product Operator if the coefficients have the following form in case of open boundary conditions

$$c_{\sigma_1,\ldots,\sigma_N;\sigma'_1,\ldots,\sigma'_N} = W^{\sigma_1,\sigma'_1} \cdots W^{\sigma_N,\sigma'_N} \tag{86}$$

for matrices W^{σ_i,σ'_i} with possibly different shapess. In Figure 11, we see the tensor diagram of an MPO with $N = 5$. Similarly to previous derivations, any operator can be written in MPO form by the same procedure with the SVD decompositions, but using the (σ_i, σ'_i) pair instead of the σ_i as indices.

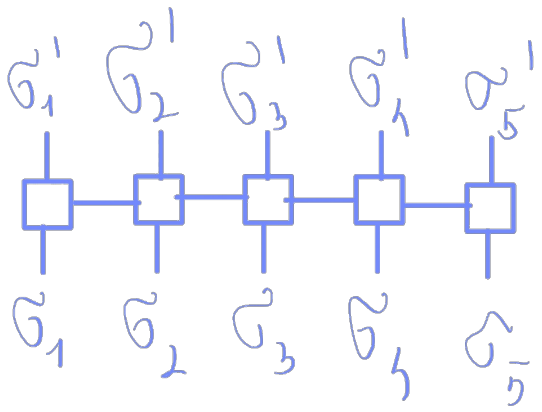

Figure 11: The tensor diagram of a Matrix Product Operator with $N = 5$.

If we apply the above written H operator to a state ψ represented by the matrices M^{σ_i}, we get the following:

$$\begin{aligned} H|\psi\rangle &= \sum_{\sigma_1,\ldots,\sigma_N,\sigma'_1,\ldots,\sigma'_N} W^{\sigma_1,\sigma'_1}\cdots W^{\sigma_N\sigma'_N} M^{\sigma'_1}\cdots M^{\sigma'_N}|\sigma_1,\ldots,\sigma_N\rangle \\ &= \sum_{\sigma_1,\ldots,\sigma_N} K^{\sigma_1}\cdots K^{\sigma_N}|\sigma_1,\ldots,\sigma_N\rangle \end{aligned} \tag{87}$$

where the K^{σ_i} matrices are defined as

$$K^{\sigma_i}_{(b_{i-1},a_{i-1}),(b_i,a_i)} = \sum_{\sigma'_i} W^{\sigma_i,\sigma'_i}_{b_{i-1},b_i} M^{\sigma'_i}_{a_{i-1},a_i}. \tag{88}$$

Which means that an MPO leaves the form of the MPS invariant, however, it increases its matrix size. In Figure 12, we see the tensor diagram of the product of an MPO and an MPS with $N = 5$ and open boundary conditions. Notice that this diagram is equivalent to the one in Figure 8.

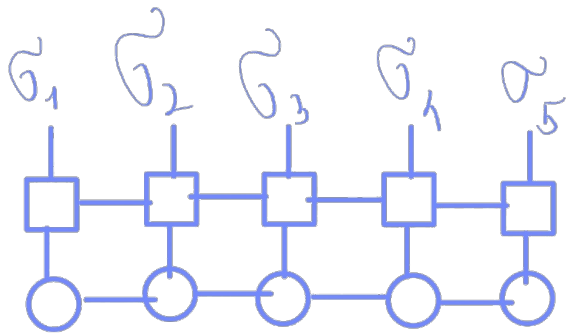

Figure 12: The tensor diagram of a Matrix Product Operator applied to a Matrix Product State with $N = 5$.

If $|\psi\rangle$ is in a mixed canonical representation

$$|\psi\rangle = \sum_{a_{l-1},a_l} |a_{l-1}\rangle_A \Psi^{\sigma_l}_{a_{l-1},a_l} |a_l\rangle_B, \tag{89}$$

the matrix elements of the operator H, after a straightforward but lengthy calculation, can be written as

$$\langle a_{l-1}\sigma_l a_l|H|a'_{l-1}\sigma'_l a'_l\rangle = \sum_{b_{l-1},b_l} L^{a_{l-1},a'_{l-1}}_{b_{l-1}} W^{\sigma_l,\sigma'_l}_{b_{l-1},b_l} R^{a_l,a'_l}_{b_l}, \tag{90}$$

where L and R are the so-called L- and R-expressions:

$$L^{a_{l-1},a'_{l-1}}_{b_{l-1}} = \sum_{\{a_i,b_i,a'_i;i<l-1\}} \prod_{k=1}^{l-1} \left(\sum_{\sigma_k,\sigma'_k} A^{\sigma_k *}_{a_{k-1},a_k} W^{\sigma_k,\sigma'_k}_{b_{k-1},b_k} A^{\sigma'_k}_{a'_{k-1},a'_k} \right) \tag{91}$$

and

$$R^{a_l,a'_l}_{b_l} = \sum_{\{a_i,b_i,a'_i;i>l\}} \prod_{k=l+1}^{L} \left(\sum_{\sigma_k\sigma'_k} B^{\sigma_k *}_{a_{k-1},a_k} W^{\sigma_k,\sigma'_k}_{b_{k-1},b_k} B^{\sigma'_k}_{a'_{k-1},a'_k} \right). \tag{92}$$

Using this, the expectation of the operator H at state $|\psi\rangle$ can be written as

$$\langle\psi|H|\psi\rangle = \sum_{\sigma_l,\sigma'_l} \sum_{a'_{l-1},a'_l} \sum_{a_{l-1},a_l} \sum_{b_{l-1},b_l} L^{a_{l-1},a'_{l-1}}_{b_{l-1}} W^{\sigma_l,\sigma'_l}_{b_{l-1},b_l} R^{a_l,a'_l}_{b_l} M^{\sigma_l *}_{a_{l-1},a_l} M^{\sigma'_l}_{a'_{l-1},a'_l}. \tag{93}$$

At this point, it might appear as a great theoretical tool useful for proofs only, but, in fact, expressing an operator in its MPO state is usually possible. To see a concrete example, let us assume that we have a chain of spins with length L, and a Hamiltonian

$$H = \sum_{i=1}^{L-1} \left(\frac{J}{2} S^+_i S^-_{i+1} + \frac{J}{2} S^-_i S^+_{i+1} + J^z S^z_i S^z_{i+1} \right) - h \sum_{i=1}^{L} S^z_i. \tag{94}$$

This form is quite compact, but to reach the MPO representation, the complete tensor product form is more convenient. In this form, the third term of the Hamiltonian is

$$\begin{aligned} H_3 = {} & J^z S^z \otimes S^z \otimes I \otimes I \ldots \otimes I \\ & + I \otimes J^z S^z \otimes S^z \otimes I \ldots \otimes I \\ & + I \otimes I \otimes J^z S^z \otimes S^z \ldots \otimes I \\ & + \ldots . \end{aligned} \tag{95}$$

To simplify further the calculation, let us introduce a new operator-valued matrices of the form

$$W^{[i]}_{b,b'} = \sum_{\sigma,\sigma'} W^{\sigma,\sigma'}_{b,b'} |\sigma\rangle\langle\sigma'|, \tag{96}$$

which acts on the i-th site's local Hilbert space. Using them, the Hamiltonian can simply be written as

$$H = W^{[1]} \cdots W^{[L]}. \tag{97}$$

To construct the operator-valued matrices $W^{[i]}$, we need to go over the possible operator combinations in the Hamiltonian. Each term contains one or two neighbouring non-identity operators, and the rest to its left and right are (possibly zero) identity operators. This means that if we go from the rightmost site, we will have (possibly zero) identity operators, then a non-identity operator, followed by either another non-identity operator or an identity operator, and finally (possibly zero) identity operators. So if we pick a site not at the edges, it can have 5 different "states":

1. there are only identity operators on the right
2. there is an S^+ on the right
3. there is an S^- on the right
4. there is an S^z on the right
5. there is a completed interaction or field term ($-hS^z$) somewhere on the right.

With these numberings, the following transitions are allowed between two neighbouring sites: $1 \to 1$ by the identity operator I; $1 \to 2$ by S^+ as that is the only way we will have exactly S^+ on the right at the next site; similarly $1 \to 3$ by S^- and $1 \to 4$ by S^z, and $1 \to 5$ by $-hS^z$, as that is the only way we can have a single non-identity operator; and we can also finish the interactions with $2 \to 5$ by $(J/2)S^-$; $3 \to 5$ by $(J/2)S^+$; $4 \to 5$ by J^zS^z; or $5 \to 5$ by the identity operator I. The matrices for the first and last sites can be constructed with the same mentality, with them being a row and column matrices respectively.

This can be formulated with the matrices

$$W^{[i]} = \begin{bmatrix} I & 0 & 0 & 0 & 0 \\ S^+ & 0 & 0 & 0 & 0 \\ S^- & 0 & 0 & 0 & 0 \\ S^z & 0 & 0 & 0 & 0 \\ -hS^z & (J/2)S^- & (J/2)S^+ & J^zS^z & I \end{bmatrix} \tag{98}$$

for $i = 2, \ldots, L-1$ and at the ends

$$W^{[1]} = \begin{bmatrix} -hS^z & (J/s)S^- & (J/2)S^+ & J^zS^z & I \end{bmatrix}, \quad W^{[L]} = \begin{bmatrix} I \\ S^+ \\ S^- \\ S^z \\ -hS^z \end{bmatrix}. \tag{99}$$

This is, of course, not exactly in the previously introduced form at this point. However, it is a substitution of the explicit representations of the appearing operators away from it.

3.4 Details of the algorithm

After the introduction of the necessary mathematical tools in the previous subsections, in this subsection we are covering the main numerical tool used in our research, the DMRG algorithm. The algorithm can be formulated in alternative ways; in this section we will show the one using Matrix Product States and Operators [47].

The goal of the algorithm is to find a state $|\psi\rangle$ that minimalizes the energy

$$E = \frac{\langle\psi|H|\psi\rangle}{\langle\psi|\psi\rangle} \tag{100}$$

for our Hamiltonian H. This can be formulated as a slightly different problem with the method of Lagrange multipliers: it is equivalent to finding the extrema of

$$\mathscr{L} = \langle\psi|H|\psi\rangle - \lambda\langle\psi|\psi\rangle. \tag{101}$$

If we substitute (74) and (93), we get a highly non-linear optimization problem in the matrix elements $M^{\sigma}_{a,a'}$. At first glance, it seems to be an impossible problem to solve, but it can be done iteratively: if we fix one but all l at a time, we will achieve a linear problem. To do this, we can take the extremum of the Lagrangian $\mathscr{L}$ with respect to $M^{\sigma_l *}_{a_{l-1},a_l}$ to achieve

$$\sum_{\sigma'_l} \sum_{a'_{l-1},a'_l} \sum_{b_{l-1},b_l} L^{a_{l-1},a'_{l-1}}_{b_{l-1}} W^{\sigma_l,\sigma'_l}_{b_{l-1},b_l} R^{a_l,a'_l}_{b_l} M^{\sigma'_l}_{a'_{l-1},a'_l} - \lambda \sum_{a'_{l-1},a'_l} \Psi^{A}_{a_{l-1},a'_{l-1}} \Psi^{B}_{a_l a'_l} M^{\sigma_l}_{a'_{l-1},a'_l} = 0. \quad (102)$$

Assuming that the sites $i = 1, \ldots, l-1$ are left-normalized, while the sites $i = l+1, \ldots, L$ are right-normalized, it can be further simplified to the core eigenvalue problem of the DMRG method

$$Jv - \lambda v = 0, \quad (103)$$

where we introduced the matrix J as

$$J_{(\sigma_l,a_{l-1},a_l),(\sigma'_l,a'_{l-1},a'_l)} = \sum_{b_{l-1},b_l} L^{a_{l-1},a'_{l-1}}_{b_{l-1}} W^{\sigma_l,\sigma'_l}_{b_{l-1},b_l} R^{a_l,a'_l}_{b_l} \quad (104)$$

and the vector v as

$$v_{(\sigma_l,a_{l-1},a_l)} = M^{\sigma_l}_{a_{l-1},a_l}. \quad (105)$$

The DMRG method implements this iterative method the following way: first, we start from an initial state

$$\psi = \sum_{\sigma} B^{\sigma_1} \cdots B^{\sigma_L} |\sigma\rangle \quad (106)$$

with right-normalization. Then, we calculate the R-expressions iteratively from $L-1$ to 1. After this, we start a so-called "sweep":

- Do a "right-sweep" from $l = 1$ to $l = L - 1$ (with increasing l by one after each one).
- Do a "left-sweep" from $l = L$ to $l = 2$ (with decreasing l by one after each one).

and repeat it until we reach the desired accuracy, which is usually quantified by the variance of the ground state energy:

$$\Delta = \langle\psi|H^2|\psi\rangle - \left(\langle\psi|H|\psi\rangle\right)^2. \quad (107)$$

A single iteration of the "right-sweep" performed at a given index l is summarized in the following steps:

- Solve the eigenproblem $Jv - \lambda v = 0$, which is equivalent to varying M^{σ_l} (which was B^{σ_l} initially, but it will loose its right-normalization during the procedure) and keeping the other matrices constant (this is usually done by the Lanczos or the Jacobi-Davidson algorithm).

- Once M^{σ_l} is obtained, we left-normalize it to A^{σ_l} with SVD. This is where the approximation happens: we have a mixed-canonical MPS, and we approximate the state by keeping only the D the biggest singular values of S, where D is referred to to as bond-dimension in the literature (using the notation from (71)).

- There will be some remaining matrices from this normalization. We multiply it to $M^{\sigma_{l+1}}$ and use it for the starting guess for the next iteration.

- We add 1 more site to the L-expression iteratively.

In the "left-sweep", similar algorithmic steps are performed as in the "right-sweep". The difference is that we right-normalize the active matrix instead, and move the "residue" into the left-most matrix. In this procedure, we also update the R-expression instead of the L-expression.

From this "recipe", we might wonder why was this method named DMRG, when the density matrices are not appearing anywhere for the first glance. However, it is there at the heart: the non-zero eigenvalues of the density matrix are equal to the singular values of the matrices during the SVDs. However, White in his original paper [46] did not use MPOs and MPSes, but used the density matrices directly to discard low-contribution states. The two methods are identical, but White used physical reasoning for the density matrix, while in this newer recipe, it comes naturally.

Finally, a few remarks about the scaling of the DMRG. Considering a lattice quantum model of N sites where each site has d degrees of freedom, the naive calculation of the ground state scales as d^{2N}. Contrary to this unfavorable exponential scaling of exact eigendecompostion, one finds that the diagonalization of the effective DMRG Hamiltonian is typically the computationally most demanding step of the DMRG procedure [53], which might still provide only an overall polynomial scaling. In particular, for low-dimensional gapped models with short-ranged interactions, DMRG scales as a modest polynomial of the retained bond dimension, i.e. it scales as ND^3. As the bond dimension D ranges between N and N^2 in most typical calculations, we find that DMRG scales as N^4 in the best case, and as N^7 in the worst case for the investigated problems.

3.5 Quantum numbers

The applied DMRG implementation is capable to treat the conserved quantum numbers of the investigated model (i.e. spin projection and particle parity) in the calculations. Taking into account these symmetries explicitly in the calculations has several advantages. It made possible for us to look for states with given quantum numbers, as well as increased the computational speed by lowering the dimension of the Hilbert space containing the solution. Another advantage of this is that states with different quantum numbers are different, so it can provide a relatively cheap (in terms of resource usage) way for computing excited states.

3.6 Initial state guesses

During our DMRG calculations, as I mentioned in the previous subsection, we needed to set up the initial state with the appropriate quantum numbers. Choosing a good initial state, however, has other advantages too, as it can speed up the calculations and avoid the possibility to find a local minimum instead of the global minimum.

As the system we applied the DMRG to was a ladder with sites on two sides containing half-spin fermions, we had chosen the initial state accordingly. This choice could be done in several ways; we decided to start with a chessboard and possibly modify some sites to achieve the desired quantum numbers. I will show one example with $N = 6$. As the

parity was a conserved quantity, we needed to construct even and odd initial states. In the case of even, we were only looking for $S = 0$ solutions, as they were the ones with the lowest energies. As the chessboard has $S_z = 0$ already, we didn't need to modify it at all. The example, with arrows indicating the spins' direction, can be see in Figure 13.

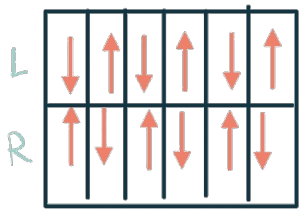

Figure 13: The even initial state for $N = 6$. The top row in the boxes represents the L side, while the bottom the R side.

The odd parity subspace was a little different, as both the $S_z = 1/2$ and $S_z = -1/2$ subspaces were containing the states we were looking for. For these two subspaces, we started from the same chessboard pattern, as it was mentioned before, but added an extra electron for one of them, and removed one for the other one, as can be seen in Figure 14.

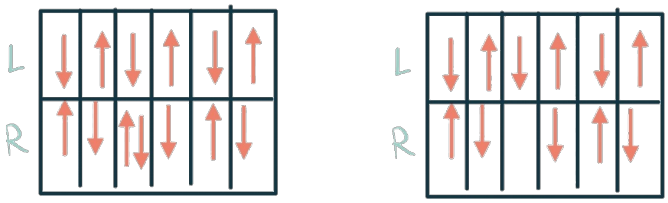

Figure 14: The odd initial states for $N = 6$. The top row in the boxes represents the L side, while the bottom the R side. The left figure is the $S_z = 1/2$, while the right is the $S_z = -1/2$.

As it was mentioned before, we were able to restrict the algorithm to a given subspace with specific quantum numbers. Because of this, we were looking for even and odd parity states separately. In the even subspace, the lowest energy states were expected to be in the $S_z = 0$ subspace, while in the odd subspace, they were expected to be in both $S_z = 1$ and $S_z = -1$ subspaces. In all of the constant S_z subspaces, calculating the n-th state (starting from $n = 1$) requires orthogonalization to the previous $n - 1$ states. This basically halves the required orthogonalization required to calculate a given amount of odd states, compared to the even ones.

This initial guess was a reasonably good start, but still far from the exact solution. At this point, the DMRG algorithm wasn't always successful in finding the global minimum, as in rare occasions, it got stuck in a local minimum. This problem could simply be solved by just calculating more excited states, as it would remove eventually the "close" local minima from the way, but it is quite costly if we do not want the higher excited states. However, the DMRG implementation we used makes it possible to add random noise to the sweeps, to avoid these problem. We found that adding a small noise to the first few sweeps has removed most of our "local minima" problems, and the remaining ones were eliminated by calculating an extra excited state (which, as a side-note, were useful to have in some cases).

3.7 Finding the excited states

The DMRG method itself is a tool for calculating the ground state of the system, but we needed excited states as well. I've already mentioned that picking different quantum numbers and conserving them is a specific method to get excited states, but they aren't general enough, as there are several orthogonal states with the same S_z. Luckily for us, there are other, not too complicated ways to get around this obstacle, for example the ITensor software circumvents it by adding the projector to the previous state to the Hamiltonian with a big enough coefficient [49]. In mathematical terms, if $|\psi_0\rangle$ is the ground state of the Hamiltonian H with energy E_0, i.e. $H|\psi_0\rangle = E_0|\psi_0\rangle$, then a new Hamiltonian H' can be defined as

$$H' = H + K|\psi_0\rangle\langle\psi_0|, \tag{108}$$

for some constant K. This new Hamiltonian will still have ψ_0 as its eigenstate, but with eigenvalue $E_0 + K$. However, this extra term will not change anything about the other eigenstates orthogonal to it. The consequence of this is that if we choose K appropriately, we can make $E_0 + K > E_1$, where E_1 is the first excited state's energy, making the first excited state the ground state of our new Hamiltonian. By default, $K = 1$ is set in the code, which was good in most of the cases, but in rare occasions, we faced an issue with the new state ψ_1 being just a rotated version of ψ_0, i.e. $\psi_1 = e^{i\phi}\psi_0$ for some $\phi \in \mathbb{R}$. In these cases, a bigger K solved the issue, at a price of a slightly slower runtime.

3.8 Maximum matrix dimension

The DMRG implementation we used provided a way to set the maximum possible dimension for the matrices in the MPS representation during the calculation (it is called "maximum link dimension", but sometimes it is also referred to as "maximum bond dimension" in the literature). The higher we go in dimensions during calculations the slower it will be in general, so it is better to keep it as low as possible. Because of this, the algorithm itself tries to use the smallest possible dimensions to achieve the desired accuracy, so this maximum isn't reached every time. However, reaching the given maximum can indicate a problem, because in this case, the algorithm might not be accurate enough to describe the given state. To avoid this possibility as much as possible, we decided to set it to 2000. This number was heuristic: during our initial calculations, we noticed that a few hundred is good in a lot of situations, but sometimes we need over 1000, however, it started to get really slow above 2000.

The maximum matrix dimension is a good indicator of the complexity of the state, as the longer the correlations are, the bigger the matrices we need to represent it accurately. At the phase borders, the correlation lengths might become divergent, which would result in singular maximum matrix dimensions. That is, we can expect to see divergent-like behaviour (as we both limit it's maximum and stop the algorithm after going below a given error) of the maximum matrix dimension at the phase borders, making it possible to create phase diagrams.

4 Synthesis

In this section, we describe a model capable of capturing the essential properties of the edge state of the topological insulators, while being moderate in size enough so that the DMRG algorithm can solve it effectively. We examine this model's ground state degeneracy, and explore its different phases in terms of interaction strength and superconducting pair potential. Finally, we characterise the degenerate ground state by local quantities.

4.1 The investigated model

As it was briefly mentioned in section 1, we wanted to create a model that can be handled efficiently by the DMRG. Because of this, we needed to construct an effectively one-dimensional system, as that is the territory where the algorithm shines. We are discussing the different parts of our interacting Hamiltonian in this subsection.

4.1.1 Ladder kinetic term

We needed a kinetic term that is quasi-one-dimensional, but in the low-energy limit, it resembles a topological insulator's edge states shown in (35). This is necessary, as the superconductor would effect the edge states of the system. This can be achieved with a ladder Hamiltonian

$$\begin{aligned} H_{\mathrm{k}} = &\sum_{n,\sigma} \begin{bmatrix} c^{\dagger}_{n,L,\sigma} & c^{\dagger}_{n,R,\sigma} \end{bmatrix} \begin{bmatrix} -\mu & t \\ t & -\mu \end{bmatrix} \begin{bmatrix} c_{n,L,\sigma} \\ c_{n,R,\sigma} \end{bmatrix} \\ &- \frac{t}{2} \sum_{n,\sigma} \left(\begin{bmatrix} c^{\dagger}_{n+1,L,\sigma} & c^{\dagger}_{n+1,R,\sigma} \end{bmatrix} \begin{bmatrix} i\sigma & 1 \\ 1 & -i\sigma \end{bmatrix} \begin{bmatrix} c_{n,L,\sigma} \\ c_{n,R,\sigma} \end{bmatrix} + \mathrm{h.c.} \right), \end{aligned} \tag{109}$$

where t is a real parameter and we introduced a new degree of freedom ζ, which we interpret as 2 sides of the ladder. Because of this, it can have two different values: L (left) and R (right). We also used the convention $\sigma = \uparrow = 1$ and $\sigma = \downarrow = -1$. In Figure 15, we have the hopping terms displayed.

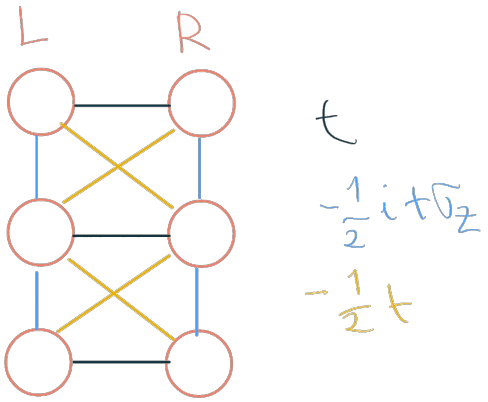

Figure 15: The hoppings in the kinetic term.

This model could be interpreted physically as a ladder construction, but for the DMRG calculations, which optimizes the problem by iterating through a list of sites, we map the Hamiltonian into a one-dimensional chain: $(1, L) \mapsto 1$, $(1, R) \mapsto 2$, ..., $(N, L) \mapsto 2N - 1$, $(N, R) \mapsto 2N$.

The Hamiltonian was constructed this way so that its low-energy continuum approximation is equivalent to the low energy continuum approximation of the edge states of the BHZ model. To prove this, we calculate the EFA for this Hamiltonian. But first, let us introduce a new vector containing the annihilation operators on the same side

$$c_n = \begin{bmatrix} c_{n,L,\uparrow} \\ c_{n,R,\uparrow} \\ c_{n,L,\downarrow} \\ c_{n,R,\downarrow} \end{bmatrix}. \tag{110}$$

With this vector, we can rewrite (109) as

$$\begin{aligned} H_{\mathrm{k}} = &\sum_n c_n^\dagger \Big(-\mu s_0 \otimes \zeta_0 + t s_0 \otimes \zeta_x \Big) c_n \\ &- \frac{t}{2} \sum_n c_{n+1}^\dagger \Big(i s_z \otimes \zeta_z + s_0 \otimes \zeta_x \Big) c_n + \mathrm{h.c.}, \end{aligned} \tag{111}$$

where we used the previously introduced notation for the Pauli-matrices: s_i is acting on the spin degree of freedom, and ζ_i is acting on the "side" degree of freedom. Taking the Fourier transform of (111), our bulk momentum-space Hamiltonian will read

$$H_{\mathrm{k}}(k) = -\mu s_0 \otimes \zeta_0 + t s_0 \otimes \zeta_x + t \sin(k) s_z \otimes \zeta_z - t \cos(k) s_0 \otimes \zeta_x. \tag{112}$$

Now we are ready to expand it around $k = 0$ to first order, achieving the low energy continuum approximation

$$H_{\mathrm{k},1}(p) = -\mu s_0 \otimes \zeta_0 + tps_z \otimes \zeta_z, \tag{113}$$

which means that the two sides are separated, as well as the two spins.

Thus, in formula (113) we verified that the low-energy physics of this ladder Hamiltonian can be identified with the one of the BHZ model's edge states, shown in (35).

4.1.2 Superconductivity

The effect of the attached superconductor can be treated in mean-field approximation by Cooper-pair creation and annihilation on the appropriate sites by the Hamiltonian

$$H_{\mathrm{sc}} = \sum_{n,\zeta} \Delta_{n,\zeta} \left[c^\dagger_{n,\zeta,\uparrow} c^\dagger_{n,\zeta,\downarrow} + \mathrm{h.c.} \right], \tag{114}$$

where the strength and the location of the superconductivity can be controlled by the parameters $\Delta_{n,\zeta}$. This term describes conventional s-wave superconductors readily available in an experimental setting. Note that this term conserves the total spin, but it does not conserve the electron number, but only the electron number parity.

4.1.3 Magnetic field

Similarly to the case of the BHZ model, we can add magnetic field to this model as well, to find Majorana Zero Modes. The magnetic field's Hamiltonian can be written as

$$H_{\mathrm{m}} = \sum_{n,\zeta} \begin{bmatrix} c^\dagger_{n,\zeta,\uparrow} & c^\dagger_{n,\zeta,\downarrow} \end{bmatrix} \left(B_{n,\zeta} \cdot s \right) \begin{bmatrix} c_{n,\zeta,\uparrow} \\ c_{n,\zeta,\downarrow} \end{bmatrix}, \tag{115}$$

where $B_{n,\zeta}$ is the three-dimensional magnetic field vector and s is the three-dimensional vector containing the 2×2 Pauli-matrices acting on the spin degree of freedom.

Both the superconductivity and the magnetic field can open a gap in the excitation spectrum, if it is added to the kinetic term, as it is shown in Figure 16 with $B_{n,\zeta} = [1, 0, 0]$ and $\Delta_{n,\zeta} = 1$. Here, we need to clarify two things. Firstly, the kinetic term alone and the kinetic term with magnetic field would not require the BdG transformation, however, it makes the comparison of spectra easier. Secondly, we can see 4 zero energy states when we apply magnetic field. However, these states are not MZMs, as they are not their own particle-hole partner, and unlike MZMs, they can be moved away from zero by applying chemical potential to the system.

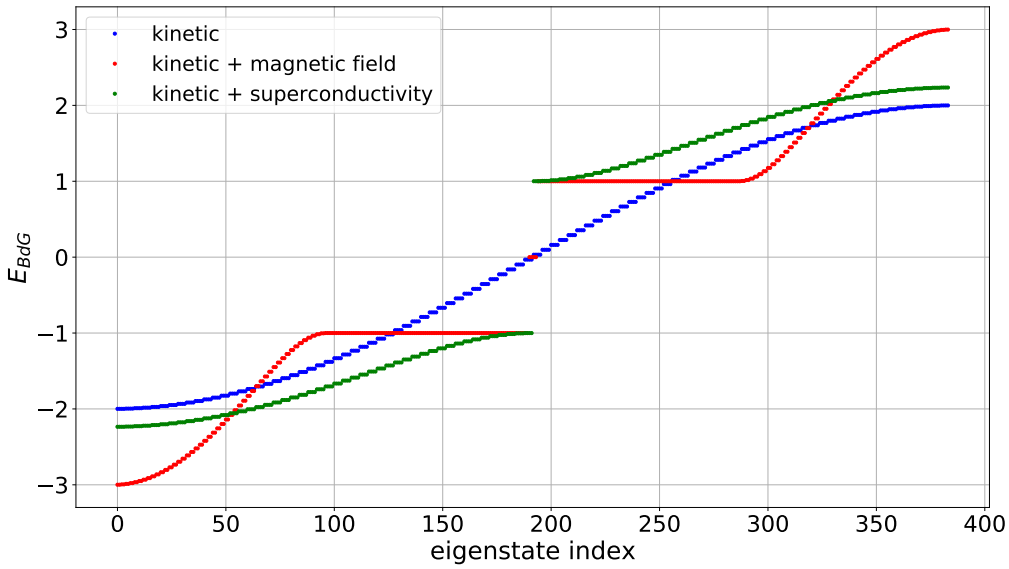

Figure 16: The BdG spectrum of the kinetic term only (blue), the kinetic term with magnetic field (red) and the kinetic term with superconductivity (green).

To see the MZMs, we can open the BdG gap in the whole system by putting magnetic field on one part of it, while superconductivity on the other one in a way that we create two domain walls. This way, the MZMs will appear at the domain walls. We can see an example in Figure 17: here, we have a ladder with length $N = 48$, with magnetic field $B_{n,\zeta} = [1, 0, 0]$ in the middle of the left side $\{n = 13, \ldots, 36\}$ and superconductivity $\Delta_{n,\zeta} = 1$ on the other parts (i.e. on the whole right side and at the bottom and top of the left side). On the left, we can see the BdG spectrum, and on the right, the probability density at each site, on both sides (the domain walls are the sites $n = 13$ and $n = 36$). We can see that the probability density peaks at the domain walls, but with an order of magnitude bigger contribution on the left side, where the domain wall actually is.

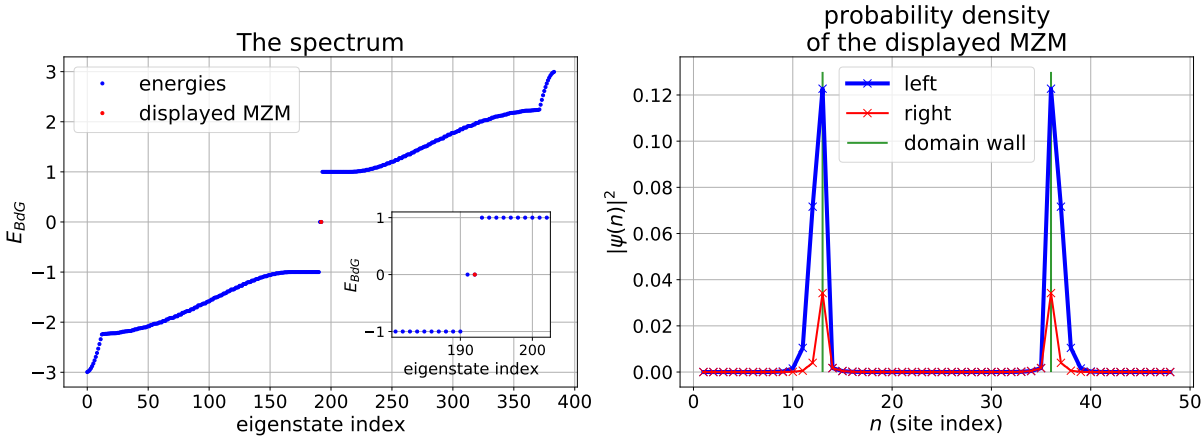

Figure 17: The BdG spectrum of a ladder (left) and the probability density of an MZM on both sides (right) with length $N = 48$, with magnetic field $B_{n,\zeta} = [1, 0, 0]$ in the middle of the left side $\{n = 13, \ldots, 36\}$ and superconductivity $\Delta_{n,\zeta} = 1$ on the other parts.

4.1.4 Interaction

Two-electron backscattering interaction can simply be implemented by flipping two adjacent, opposite spins, as it changes their propagating direction. That is, the interaction can be defined as

$$H_{\text{int}} = \sum_{n,\zeta} V_{n,\zeta} \left[c^\dagger_{n,\zeta,\uparrow} c_{n,\zeta,\downarrow} c^\dagger_{n+1,\zeta,\downarrow} c_{n+1,\zeta,\uparrow} + \text{h.c.} \right], \tag{116}$$

where $V_{n,\zeta}$ are real parameters, characterising the interaction. Note that this term is slightly different than the interaction sketched in Figure 2. They both conserve the electron number, but the interaction (116) conserves the total spin as well.

4.1.5 The complete model

For our complete model, we took the ladder kinetic Hamiltonian (109) and added superconductivity with (114) and interaction of the form (116), i.e. the systems we examined had their Hamiltonians of the form

$$H = H_{\text{k}} + H_{\text{sc}} + H_{\text{int}}. \tag{117}$$

4.1.6 Different configurations

We've examined two different configurations denoted by configuration A and B. For configuration A, we put constant superconductivity on the right side, i.e. $\Delta_{m,\zeta} = \delta_{\zeta,R}\Delta$ (where Δ is a real constant and not the matrix with elements $\Delta_{m,\zeta}$), and interaction on the left side, i.e. $V_{m,\zeta} = \delta_{\zeta,L}V$ (where V is a real constant and not the matrix with elements $V_{m,\zeta}$). For configuration B, we stayed with the superconducting right side, i.e. $\Delta_{m,R} = \Delta$, but "replaced" the interaction on the two edges of the left side with superconductivity, creating two domain walls. More formally, for an appropriately small p, we set

$$\Delta_{m,L} = \Delta \sum_{i=1}^{p} \left(\delta_{m,i} + \delta_{m,N+1-i} \right) \tag{118}$$

and

$$V_{m,L} = V \sum_{i=p}^{N-p} \delta_{m,i}, \tag{119}$$

i.e. there are p sites at both ends of the left side with superconductivity, and every site between them (including the middle most superconducting sites) are connected by interaction. For $N = 8$ and $p = 3$, the two configurations can be seen in Figure 18, with the kinetic terms not shown.

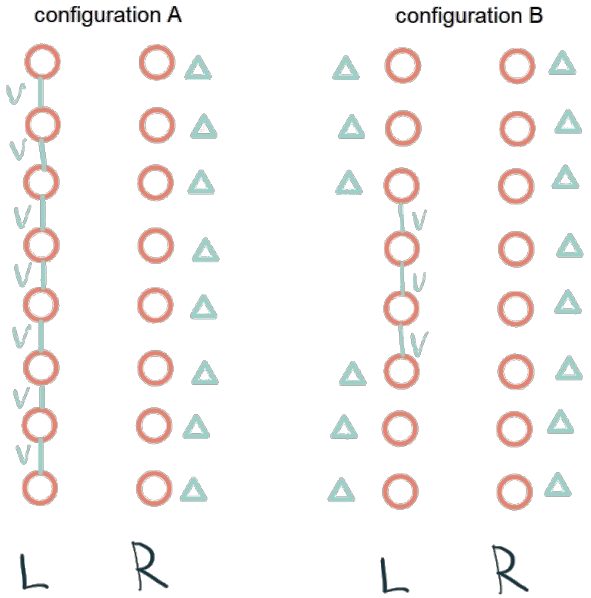

Figure 18: Sketch of configuration A (left) and configuration B (right) for $N = 8$ and $p = 3$, without the kinetic term.

For both configuration A and B, we set $t = 1$, i.e. we measured everything in units of t. Although we only report here results obtained for $\mu = 0$, further calculations show that the discovered degenerate ground state remains intact at finite chemical potential.

4.2 DMRG spectrum

Our exploration started with the ground state degeneracy of configuration A. In figure Figure 19, we see the first 7 excitation energies our model with fixed $\Delta = 0.7$ and $N = 20$, as a function of V We see that there is an interval around $V \approx 1.75$, where the ground state is 4-fold degenerate, and the first excited state is at least 4-fold degenerate. Even though we don't show it here, we have that the region with small interactions behaves like a metal, i.e. states are getting denser and denser as system size increases.

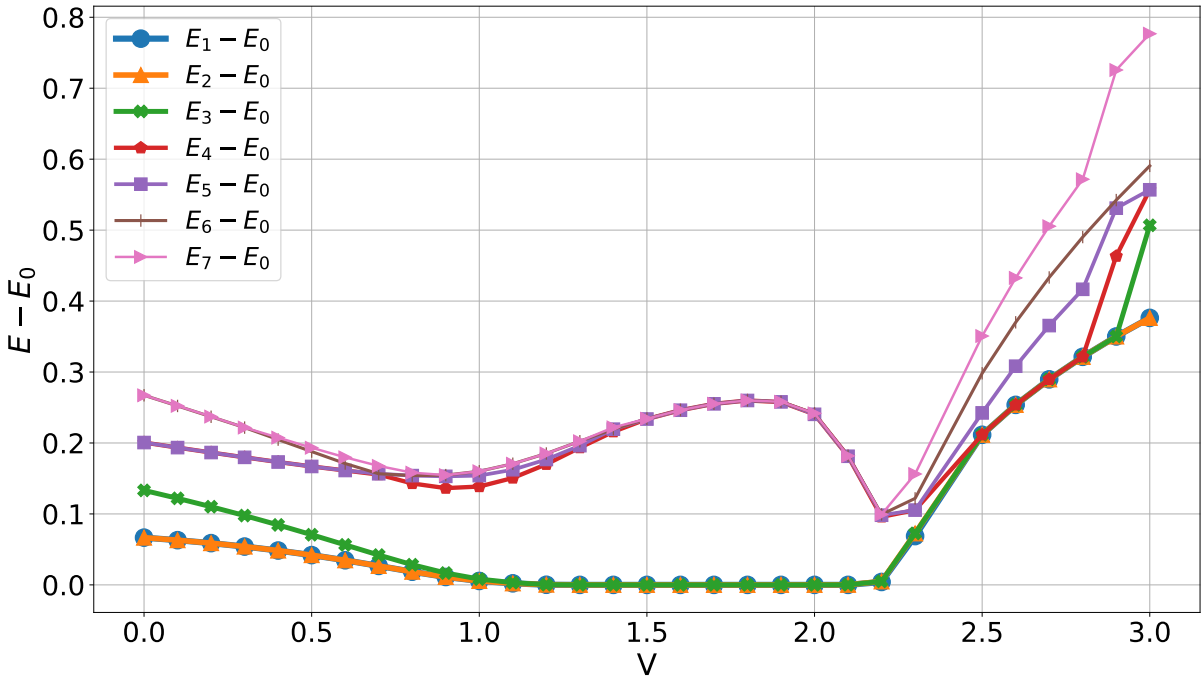

Figure 19: The first 7 excitation energies of our model with fixed $\Delta = 0.7$ and $N = 20$, as a function of V.

To examine further the degeneracy in the middle region, the next step was to check how the degeneracy behaves as the system gets bigger and bigger. And, as we expected, the degeneracy of the first 4 states, as well as the next fours, gets exponentially exact as the size increases. This process is shown in Figure 20 for $V = 1.6$ and $\Delta = 0.7$.

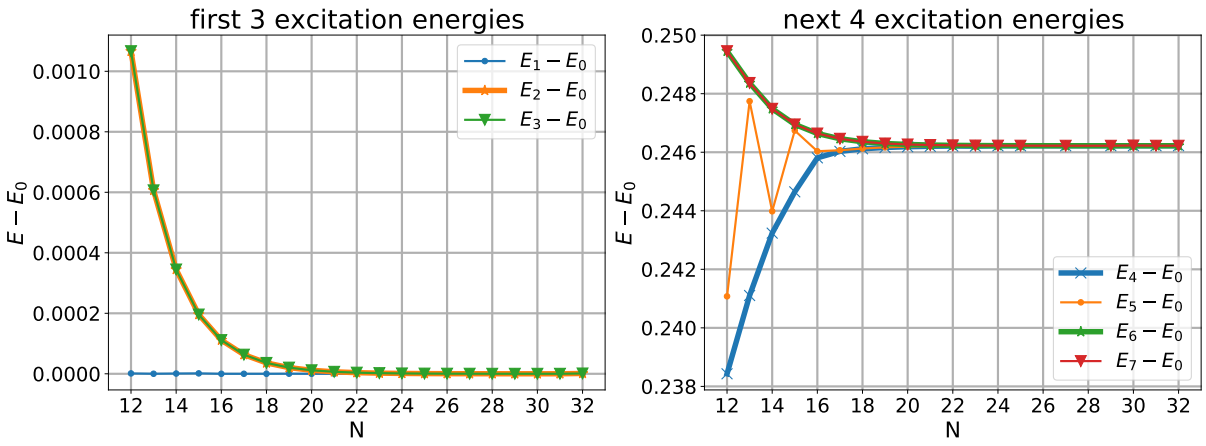

Figure 20: The first 3 excitation energies (left) and the next 4 excitation energies (right) as a function of the model length N with $V = 1.6$ and $\Delta = 0.7$.

4.3 2D phase diagram

To examine the different phases of the system, we can look at the standard deviation of the 4 lowest energies. This is a good indicator of the presence of the 4-fold degeneracy in the sense that the standard deviation is zero if and only if they are all equal. An interesting "byproduct" of the necessary DMRG calculations is the maximum matrix dimension during the sweeps, for a given set of parameters. As it was mentioned in subsection 3.8, it can be used to elucidate a phase diagram as a big maximum matrix dimension is an indicator of divergent correlation lengths. In Figure 21 we see the previously mentioned standard deviation as a function of the two system parameters Δ and V and the maximum matrix dimension of the lowest energy even parity state as a function of the same system parameters.

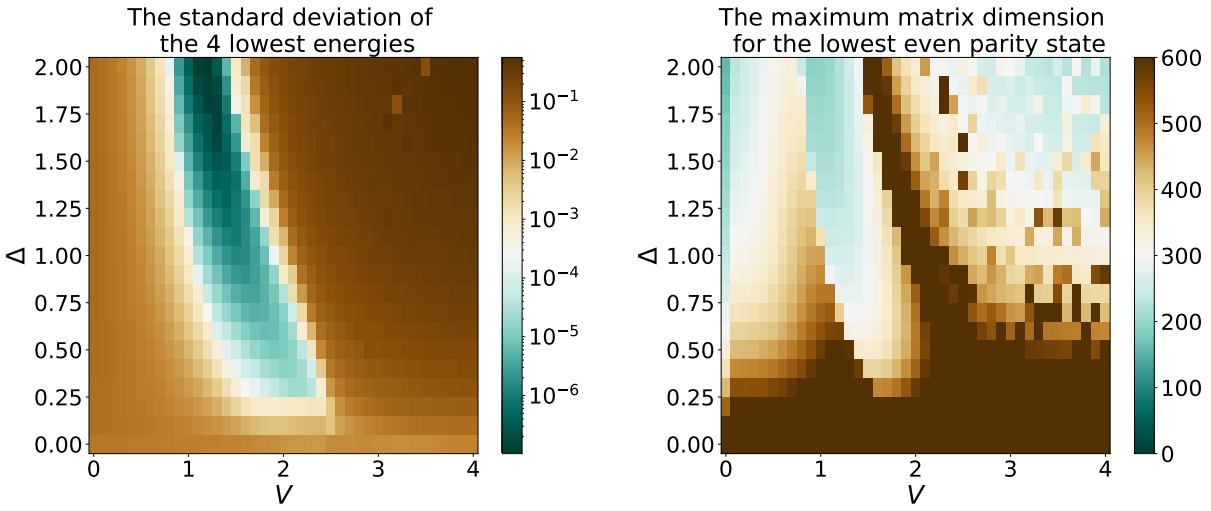

Figure 21: The standard deviation of the 4 lowest energies (left) and the maximum matrix dimension of the lowest energy even parity state (right) as a function of the system parameters.

In Figure 21 we find that in the investigated domain of $(V, \Delta) \in [0, 4] \times [0, 2]$, the system has several distinct phases according to the maximum matrix dimension analysis. More importantly, in the middle section, the ground state is at least fourfold degenerate, implying a possibility to have parafermions there.

4.4 Local quantities

The next thing to examine is configuration B with domain walls. For this, we picked a point inside the middle section of the phase diagram, namely $\Delta = 0.7$ and $V = 1.75$, and we set the length of the ladder to $N = 48$, with $p = 12$.

In this case, the ground state is four-fold degenerate, with 1 electron in each site in all four ground states, in the sense that

$$\langle \psi_i | c^\dagger_{m,\zeta,\uparrow} c_{m,\zeta,\uparrow} + c^\dagger_{m,\zeta,\downarrow} c_{m,\zeta,\downarrow} | \psi_j \rangle = \delta_{i,j} \tag{120}$$

for the four degenerate ground states $\{\psi_1, \psi_2, \psi_3, \psi_4\}$, both sides $\zeta \in \{L, R\}$ and all sites $m = 1, \ldots, N$. This means that the four different ground states cannot be distinguished by means of local electric probes. Note that this indistinguishability is present in non-zero chemical potential as well, but the equality in (120) is replaced by proportionality. However, looking at the magnetization, as it can be seen in Figure 22, we are able to

distinguish the four ground states: on the left side of the ladder, where we have the two domain walls, they have two big peaks, with different signs. It also effects the right side of the ladder, due to the connection via the kinetic term, but it is 2 orders of magnitude smaller. This difference in the magnetization has a serious consequence: the fourfold degeneracy can be broken by external magnetic field (which would also break the TRS).

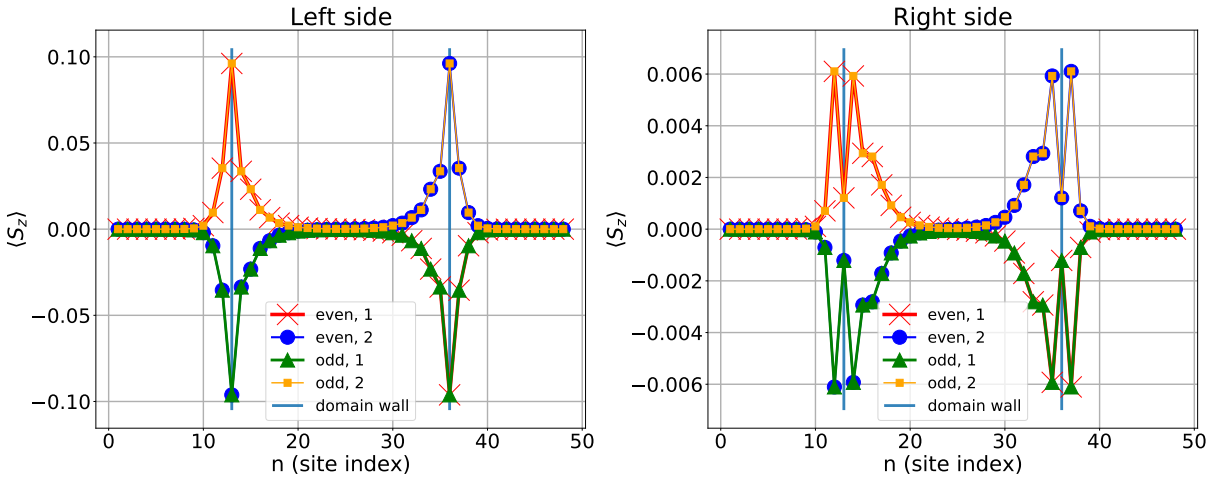

Figure 22: The magnetization of the fourfold degenerate ground state on the two sides of the ladder with configuration B.

We also look at the matrix elements of the annihilation/creation operators between two distinct states. Figure 23 shows that if we put in (or remove) an electron in (from) the initial state, where will it show up in (disappear from) the final state. And, as it turns out, these quantities are a good indicator of the localization of the MZMs [54], and for parafermions as well, by using similar arguments.

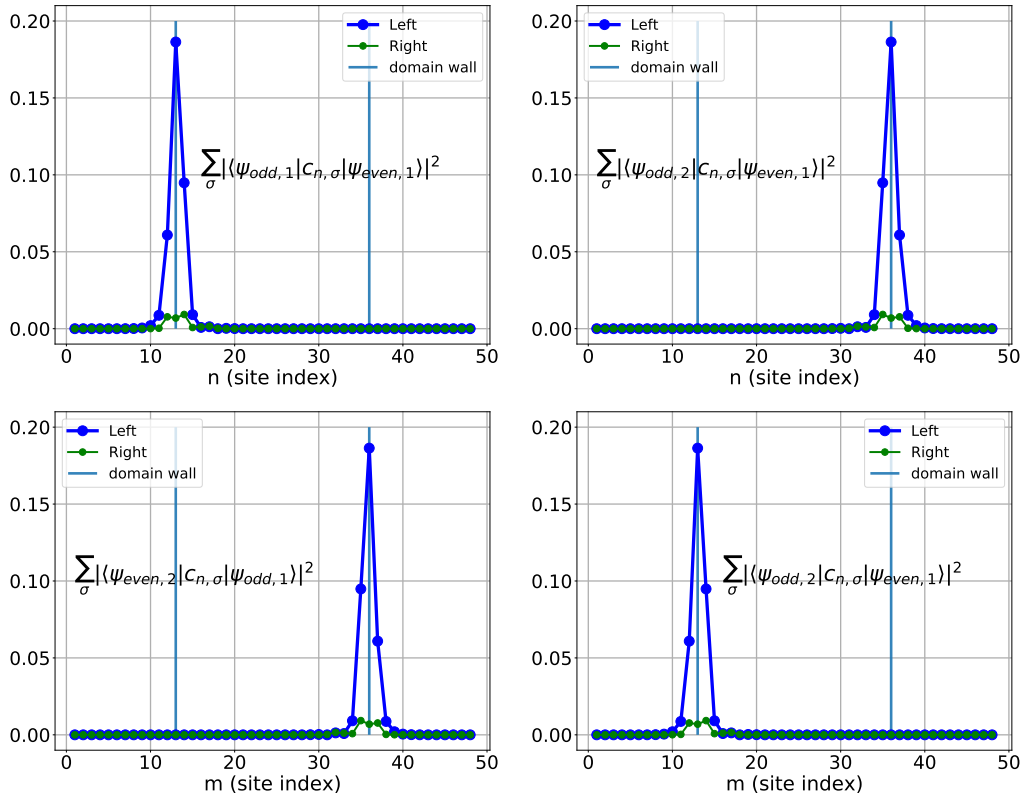

Figure 23: The matrix elements of the annihilation/creation operators with the fourfold degenerate ground states with configuration B.

4.5 Interpretation

Our results suggest that with moderately strong interaction, we have the fourfold degeneracy required to observe parafermions. The degenerate ground states are protected against electrostatic noises, in the sense that the degeneracy cannot be broken by electrostatic potential. Even though we did not show it explicitly, this protection is present when we have non-zero chemical potential as well. Both the magnetic expectations shown in Figure 22 and the matrix elements of the annihilation/creation operators shown in Figure 23 affirms that the degenerate ground states are located at the domain walls. These are promising signs for parafermions, but they are not enough to be 100% certain about it. Another possibility could be that the excitations at the interfaces are not parafermions, but Majorana Kramers doublets, as they can show similar signatures [55]. To decide between the two possibilities, we will need to do more characterisations, for example we will need to analyse the Josepson current between two separate superconductor parts.

5 Summary and outlook

In this thesis, we looked at how to create Majorana zero modes on the edge states of topological insulators with the BdG formalism. We introduced an effective microscopic model, which can possibly host, in the presence of strong interaction, parafermions, the generalization of the Majorana zero modes. We found convincing signs for the existence of those parafermions with DMRG calculations. We also created a phase diagram for our model as a function of the strengths of the superconductivity and the interaction, and identified a parameter region with fourfold degeneracy. Finally, we characterized these fourfold degenerate ground states by local quantities and showed that these excitations are localized at the interface of superconducting and interacting regions, with topological protection.

In the future, we are planning to continue this research, hence we have already laid out the direction of our exploration. We are planning to completely characterize the presented exotic states, for example by studying Josephson currents. We are also going to try several other interaction terms. An interesting choice is

$$H_{\text{int}} = \sum_{n,\zeta} V_{n,\zeta} \left[c^{\dagger}_{n,\zeta,\uparrow} c_{n,\zeta,\downarrow} c^{\dagger}_{n+1,\zeta,\uparrow} c_{n+1,\zeta,\downarrow} + \text{h.c.} \right], \tag{121}$$

which, similarly to our current one defined in (116), flips spins in neighbouring sites, but instead of flipping two opposite ones, it flips two identical ones. Note that this is the interaction sketched in Figure 2. And finally, we are also going to study how the decoherence due to excited states impacts logical qubits defined in the ground state during the movement of the interface region required for braiding. This time evolution will also be simulated by matrix product states [56].

6 Acknowledgements

First and foremost, I would like to express my appreciation to my supervisors, Gergely Barcza and László Oroszlány for your support and guidance over the years. I feel really lucky to have you as my supervisors, as both of you are a great person and an excellent researcher.

I would also like to thank my family for their immense love and vast support. You are always there for me and you are going above and beyond every time to help me. I am really grateful to you.

This research was supported by the Ministry of Innovation and Technology and the National Research, Development and Innovation Office within the Quantum Information National Laboratory of Hungary.

The support from the Student Scholarship of the Wigner Research Center for Physics is also greatly acknowledged.

We acknowledge KIFÜ for awarding us access to resource based in Hungary at Debrecen.

References

[1] J. M. Kosterlitz and D. J. Thouless. Ordering, metastability and phase transitions in two-dimensional systems. *Journal of Physics C: Solid State Physics*, 6(7):1181–1203, April 1973.

[2] R. B. Laughlin. Quantized Hall conductivity in two dimensions. *Physical Review B*, 23(10):5632, May 1981.

[3] M. Z. Hasan and C. L. Kane. Colloquium: Topological insulators. *Reviews of Modern Physics*, 82(4):3045–3067, November 2010.

[4] A. A. Burkov, M. D. Hook, and Leon Balents. Topological nodal semimetals. *Physical Review B*, 84(23):235126, December 2011.

[5] Masatoshi Sato and Yoichi Ando. Topological superconductors: a review. *Reports on Progress in Physics*, 80(7):076501, May 2017.

[6] N. P. Armitage, E. J. Mele, and Ashvin Vishwanath. Weyl and dirac semimetals in three-dimensional solids. *Reviews of Modern Physics*, 90:015001, Jan 2018.

[7] Janos K. Asboth, László Oroszlány, and András Pályi. *A short course on topological insulators: band-structure and edge states in one and two dimensions*. Springer Berlin Heidelberg, New York, NY, 2016.

[8] Joseph Maciejko, Xiao-Liang Qi, H. Dennis Drew, and Shou-Cheng Zhang. Topological quantization in units of the fine structure constant. *Phys. Rev. Lett.*, 105:166803, Oct 2010.

[9] Christoph Brüne, Andreas Roth, Hartmut Buhmann, Ewelina M. Hankiewicz, Laurens W. Molenkamp, Joseph Maciejko, Xiao-Liang Qi, and Shou-Cheng Zhang. Spin polarization of the quantum spin hall edge states. *Nature Physics*, 8(6):485–490, May 2012.

[10] Ibm quantum | use cases. `https://web.archive.org/web/20210412232240/https://www.ibm.com/quantum-computing/learn/welcome/`. Accessed: 2022. Jan. 18.

[11] Frank Arute, Kunal Arya, Ryan Babbush, Dave Bacon, Joseph C. Bardin, Rami Barends, Rupak Biswas, Sergio Boixo, Fernando G. S. L. Brandao, David A. Buell, Brian Burkett, Yu Chen, Zijun Chen, Ben Chiaro, Roberto Collins, William Courtney, Andrew Dunsworth, Edward Farhi, Brooks Foxen, Austin Fowler, Craig Gidney, Marissa Giustina, Rob Graff, Keith Guerin, Steve Habegger, Matthew P. Harrigan, Michael J. Hartmann, Alan Ho, Markus Hoffmann, Trent Huang, Travis S. Humble, Sergei V. Isakov, Evan Jeffrey, Zhang Jiang, Dvir Kafri, Kostyantyn Kechedzhi, Julian Kelly, Paul V. Klimov, Sergey Knysh, Alexander Korotkov, Fedor Kostritsa, David Landhuis, Mike Lindmark, Erik Lucero, Dmitry Lyakh, Salvatore Mandrà, Jarrod R. McClean, Matthew McEwen, Anthony Megrant, Xiao Mi, Kristel Michielsen, Masoud Mohseni, Josh Mutus, Ofer Naaman, Matthew Neeley, Charles Neill, Murphy Yuezhen Niu, Eric Ostby, Andre Petukhov, John C. Platt, Chris Quintana, Eleanor G. Rieffel, Pedram Roushan, Nicholas C. Rubin, Daniel Sank, Kevin J. Satzinger, Vadim Smelyanskiy, Kevin J. Sung, Matthew D. Trevithick, Amit Vainsencher, Benjamin Villalonga, Theodore White, Z. Jamie Yao, Ping Yeh, Adam Zalcman, Hartmut Neven, and John M. Martinis. Quantum supremacy using a programmable superconducting processor. *Nature*, 574(7779):505–510, October 2019.

[12] John Preskill. Quantum Computing in the NISQ era and beyond. *Quantum*, 2:79, August 2018.

[13] A Yu Kitaev. Unpaired majorana fermions in quantum wires. *Physics-Uspekhi*, 44(10S):131–136, oct 2001.

[14] Paul Wiegmann. Topological superconductivity. *Progress of Theoretical Physics Supplement*, 107:243–279, 1992.

[15] Jason Alicea. New directions in the pursuit of majorana fermions in solid state systems. *Reports on Progress in Physics*, 75(7):076501, jun 2012.

[16] C.W.J. Beenakker. Search for majorana fermions in superconductors. *Annual Review of Condensed Matter Physics*, 4(1):113–136, 2013.

[17] Barbara M. Terhal. Quantum error correction for quantum memories. *Rev. Mod. Phys.*, 87:307–346, Apr 2015.

[18] V. Mourik, K. Zuo, S. M. Frolov, S. R. Plissard, E. P. A. M. Bakkers, and L. P. Kouwenhoven. Signatures of majorana fermions in hybrid superconductor-semiconductor nanowire devices. *Science*, 336(6084):1003–1007, May 2012.

[19] Ramón Aguado and Leo P. Kouwenhoven. Majorana qubits for topological quantum computing. *Physics Today*, 73(6):44–50, June 2020.

[20] A.Yu. Kitaev. Fault-tolerant quantum computation by anyons. *Annals of Physics*, 303(1):2–30, January 2003.

[21] Alexei Kitaev. Anyons in an exactly solved model and beyond. *Annals of Physics*, 321(1):2–111, January 2006.

[22] Olivér Kürtössy, Zoltán Scherübl, Gergö Fülöp, István Endre Lukács, Thomas Kanne, Jesper Nygård, Péter Makk, and Szabolcs Csonka. Andreev molecule in parallel InAs nanowires. *Nano Letters*, 21(19):7929–7937, September 2021.

[23] Liang Fu and C. L. Kane. Superconducting proximity effect and majorana fermions at the surface of a topological insulator. *Phys. Rev. Lett.*, 100:096407, Mar 2008.

[24] Johan Nilsson, A. R. Akhmerov, and C. W. J. Beenakker. Splitting of a cooper pair by a pair of majorana bound states. *Phys. Rev. Lett.*, 101:120403, Sep 2008.

[25] Liang Fu and C. L. Kane. Josephson current and noise at a superconductor/quantum-spin-hall-insulator/superconductor junction. *Phys. Rev. B*, 79:161408, Apr 2009.

[26] Masatoshi Sato, Yoshiro Takahashi, and Satoshi Fujimoto. Non-abelian topological order in s-wave superfluids of ultracold fermionic atoms. *Phys. Rev. Lett.*, 103:020401, Jul 2009.

[27] Jay D. Sau, Roman M. Lutchyn, Sumanta Tewari, and S. Das Sarma. Generic new platform for topological quantum computation using semiconductor heterostructures. *Phys. Rev. Lett.*, 104:040502, Jan 2010.

[28] Jason Alicea. Majorana fermions in a tunable semiconductor device. *Phys. Rev. B*, 81:125318, Mar 2010.

[29] Roman M. Lutchyn, Jay D. Sau, and S. Das Sarma. Majorana fermions and a topological phase transition in semiconductor-superconductor heterostructures. *Phys. Rev. Lett.*, 105:077001, Aug 2010.

[30] Jason Alicea and Paul Fendley. Topological phases with parafermions: Theory and blueprints. *Annual Review of Condensed Matter Physics*, 7(1):119–139, 2016.

[31] Jelena Klinovaja, Amir Yacoby, and Daniel Loss. Kramers pairs of majorana fermions and parafermions in fractional topological insulators. *Physical Review B*, 90(15), October 2014.

[32] Roman M. Lutchyn, Jay D. Sau, and S. Das Sarma. Majorana fermions and a topological phase transition in semiconductor-superconductor heterostructures. *Physical Review Letters*, 105(7), August 2010.

[33] Maissam Barkeshli, Chao-Ming Jian, and Xiao-Liang Qi. Twist defects and projective non-abelian braiding statistics. *Physical Review B*, 87(4), January 2013.

[34] Maissam Barkeshli and Xiao-Liang Qi. Synthetic topological qubits in conventional bilayer quantum hall systems. *Physical Review X*, 4(4), November 2014.

[35] Christoph P. Orth, Rakesh P. Tiwari, Tobias Meng, and Thomas L. Schmidt. Non-abelian parafermions in time-reversal-invariant interacting helical systems. *Phys. Rev. B*, 91:081406, Feb 2015.

[36] David Aasen, Michael Hell, Ryan V. Mishmash, Andrew Higginbotham, Jeroen Danon, Martin Leijnse, Thomas S. Jespersen, Joshua A. Folk, Charles M. Marcus, Karsten Flensberg, and Jason Alicea. Milestones toward majorana-based quantum computing. *Phys. Rev. X*, 6:031016, Aug 2016.

[37] Jason Alicea, Yuval Oreg, Gil Refael, Felix von Oppen, and Matthew P. A. Fisher. Non-abelian statistics and topological quantum information processing in 1d wire networks. *Nature Physics*, 7(5):412–417, February 2011.

[38] Sankar Das Sarma, Michael Freedman, and Chetan Nayak. Majorana zero modes and topological quantum computation. *npj Quantum Information*, 1(1), October 2015.

[39] Fan Zhang and C. L. Kane. Time-reversal-invariant Z_4 fractional josephson effect. *Phys. Rev. Lett.*, 113:036401, Jul 2014.

[40] Paul Fendley. Parafermionic edge zero modes in Z_n-invariant spin chains. *Journal of Statistical Mechanics: Theory and Experiment*, 2012(11):P11020, nov 2012.

[41] Adrian Hutter and Daniel Loss. Quantum computing with parafermions. *Phys. Rev. B*, 93:125105, Mar 2016.

[42] Eugen Wigner. *Gruppentheorie und ihre Anwendung auf die Quantenmechanik der Atomspektren*. Vieweg+Teubner Verlag, 1931.

[43] Xiao-Liang Qi, Yong-Shi Wu, and Shou-Cheng Zhang. Topological quantization of the spin hall effect in two-dimensional paramagnetic semiconductors. *Phys. Rev. B*, 74:085308, Aug 2006.

[44] C. L. Kane and E. J. Mele. Z_2 topological order and the quantum spin hall effect. *Phys. Rev. Lett.*, 95:146802, Sep 2005.

[45] Alexander Weiße, Gerhard Wellein, Andreas Alvermann, and Holger Fehske. The kernel polynomial method. *Rev. Mod. Phys.*, 78:275–306, Mar 2006.

[46] Steven R. White. Density matrix formulation for quantum renormalization groups. *Phys. Rev. Lett.*, 69:2863–2866, Nov 1992.

[47] Ulrich Schollwoeck. The density-matrix renormalization group in the age of matrix product states. *Annals of Physics - ANN PHYS N Y*, 326, 08 2010.

[48] Örs Legeza, Libor Veis, and Tamas Mosoni. QC-DMRG-Budapest, a program for model and ab initio DMRG calculations, 2020.

[49] Matthew Fishman, Steven R. White, and E. Miles Stoudenmire. The ITensor software library for tensor network calculations, 2020.

[50] Carl Eckart and Gale Young. The approximation of one matrix by another of lower rank. *Psychometrika*, 1(3):211–218, September 1936.

[51] Stellan Östlund and Stefan Rommer. Thermodynamic limit of density matrix renormalization. *Phys. Rev. Lett.*, 75:3537–3540, Nov 1995.

[52] Jacob C Bridgeman and Christopher T Chubb. Hand-waving and interpretive dance: an introductory course on tensor networks. *Journal of Physics A: Mathematical and Theoretical*, 50(22):223001, may 2017.

[53] Csaba Nemes, Gergely Barcza, Zoltán Nagy, Örs Legeza, and Péter Szolgay. The density matrix renormalization group algorithm on kilo-processor architectures: Implementation and trade-offs. *Computer Physics Communications*, 185(6):1570–1581, 2014.

[54] E. M. Stoudenmire, Jason Alicea, Oleg A. Starykh, and Matthew P.A. Fisher. Interaction effects in topological superconducting wires supporting majorana fermions. *Phys. Rev. B*, 84:014503, Jul 2011.

[55] Aaron Chew, David F. Mross, and Jason Alicea. Fermionized parafermions and symmetry-enriched majorana modes. *Phys. Rev. B*, 98:085143, Aug 2018.

[56] Sebastian Paeckel, Thomas Köhler, Andreas Swoboda, Salvatore R. Manmana, Ulrich Schollwöck, and Claudius Hubig. Time-evolution methods for matrix-product states. *Annals of Physics*, 411:167998, December 2019.